RSC Advances

PAPER

View Article Online
View Journal | View Issue

Cite this: *RSC Adv.*, 2026, **16**, 18475

Ni^{2+}-doped magnesium aluminosilicate nanoceramics: structural, optical, dielectric, and antimicrobial properties

A. M. Mansour, [a] Mohamed I. Farouk,[b] A. G. Darwish [c] and Ali B. Abou Hammad *[a]

Herein, nanospheres of Ni^{2+}-doped magnesium aluminosilicate (MAS) glass-ceramics were produced utilizing a sol–gel processing technique in order to examine the impact of the incorporation of different levels of Ni (0, 1, 2, 3, 4, or 5 mol%) on their structural, optical, electrical and antimicrobial characteristics. X-ray diffraction analysis revealed that the samples predominantly consist of two polycrystalline phases: hexagonal $Mg_2Al_4Si_5O_{18}$ and orthorhombic Mg_2SiO_4; as the level of Ni^{2+} incorporation increased, more and more prominent orthorhombic reflections became apparent. It was found from the examination of electron micrographs that the average crystallite diameter was approximately 23 nm and that the particles were nearly spherical with diameters between 20 and 30 nm, exhibiting a uniform dispersion of Ni throughout the MAS matrix. Optical diffuse reflectance (DR) spectra demonstrated that all of the studied samples contained the characteristic absorption features associated with Ni^{2+} ions coordinated to six oxygen atoms and that the optical band gap of Ni(doped)-MAS varied non-linearly with respect to the increasing amounts of Ni, which can be explained by the existence of the defect states that are created by dopant incorporation and/or changes that occur in the electronic structure. At temperatures of 30 °C, 60 °C, and 100 °C, dielectric measurements exhibited stable high-frequency permittivity values (≈15–20) for all sample compositions measured, indicating significant dependence on Ni. At low frequencies and temperatures, dielectric measurements indicate that the MAS-1Ni sample has an extraordinarily high permittivity value of 5.12×10^4 at 0.1 Hz and 100 °C. The antimicrobial assessment of Gram-positive and Gram-negative bacteria and fungi samples demonstrated visible clear inhibition zones (max 18 mm) as a result of the continuous release of Ni^{2+} ions and the alteration of the cell wall structure in microbial organisms. These findings demonstrate that MAS glass-ceramic nanospheres modified with Ni have the ability to offer tunable multifunctional properties, making them promising candidates for biomedical, antimicrobial and functional ceramic applications.

Received 20th February 2026
Accepted 25th March 2026

DOI: 10.1039/d6ra01509c

rsc.li/rsc-advances

1 Introduction

In recent years, an advanced class of surface-active bioglass-ceramics and bioceramics comprising bioactive silicates has emerged as suitable candidates for hard tissue regeneration. Multifunctional ceramic nanostructured materials have received significant attention from researchers because they are useful for fabricating biomedical devices, electronic devices/components, and antimicrobial systems.[1] One type of ceramic that has been identified as a good candidate for multifunctional ceramic nanostructured materials is magnesium aluminosilicate (MAS) glass-ceramics because of their good chemical durability/thermal stability, biocompatibility, and tunable physicochemical properties.[2] These ceramics also possess unique physical/chemical properties that can be enhanced further *via* the controlled incorporation of transition metal ions, thereby allowing for the development of advanced materials with specific optical, dielectric, and biological characteristics.[3]

The recent advances in ceramic materials have highlighted the critical role of compositional design and microstructural engineering in tailoring the functional properties. For instance, grain boundary modification through SiO_2 doping has been shown to effectively suppress grain growth and enhance mechanical strength in silicate-based ceramics by controlling diffusion processes and stress distribution.[4] Similarly, dopant-induced modifications in oxide ceramics have demonstrated significant improvements in structural integrity and electrical performance, where multi-component doping strategies reduce

[a]*Solid State Physics Department, Physics Research Institute, National Research Centre, 33 El-Bohouth St., Dokki, Giza, 12622, Egypt. E-mail: abohmad2@yahoo.com*
[b]*College of Engineering, Deanship of Scientific Research, Imam Mohammad Ibn Saud Islamic University (IMSIU), Riyadh 11432, Saudi Arabia*
[c]*Microwave Physics and Dielectrics Department, Physics Research Institute, National Research Centre, 33 El-Bohouth St., Dokki, Giza, 12622, Egypt*

defects and enhance phase stability.[5] In addition, the precise control of microstructure and pore architecture has been achieved through advanced processing routes, leading to enhanced functionality in ceramic membranes and related systems.[6]

Furthermore, emerging synthesis approaches such as microwave-assisted methods enable the rapid formation of defect-rich ceramic systems with improved dielectric and electromagnetic properties due to enhanced lattice distortion and homogeneous element distribution.[7] In high-temperature applications, nanostructured silicate-based coatings have shown superior resistance to corrosive environments through controlled phase evolution and protective layer formation.[8] Moreover, transition metal-based nanocomposites have demonstrated enhanced catalytic and functional performance *via* defect-mediated mechanisms and reactive species generation.[9]

Akermanite ($Ca_2MgSi_2O_7$), wollastonite ($CaSiO_3$), bredigite ($Ca_7MgSi_4O_{16}$), larnite (Ca_2SiO_4), and diopside ($CaMgSi_2O_6$) are some of the silicate-based materials that are known for their bioactivity.[10] Cordierite ($Mg_2Al_4Si_5O_{18}$) and forsterite (Mg_2SiO_4) are examples of magnesium aluminosilicates that have been studied by many researchers because of their low coefficient of thermal expansion, high strength, and good insulating properties.[11] The crystallization behavior and the phase composition of the glass-ceramic made from MAS can be modified based on the synthesis parameters and chemical composition, thus exhibiting the optimal properties for a particular application.[12] The nanostructured forms of these types of materials also provide the advantages of increased surface area, enhanced reactivity, and unique quantum confinement effects on their optical and electronic properties.[13] However, further structural investigations are needed to assess the suitability of active silicate systems for various applications.

Among these materials, the forsterite-based (Mg_2SiO_4) system has emerged as a promising bioceramic alternative, characterized by a favorable electronic structure, chemical stability, and bonding configuration, where variations in charge distribution and defect states influence interfacial reactions with biological tissues.[14,15] These effects are effectively elucidated through spectroscopic techniques, which reveal the structural–property relationships that govern optical, electrical, and biological responses and functional performance in adsorption, electronic, water softening, catalysis, and sensing-related biomedical devices.[14,15]

The inclusion of transition metals into ceramic matrices is an effective way of modifying the material properties.[16] Specifically, nickel (Ni^{2+}) is particularly interesting due to its octahedral coordination sites in the oxide lattice, creating unique optical absorption touchstones and, therefore, changes in the band structure of the material.[17] Ni^{2+} doping will also affect the crystallization, defect chemistry, and ionic conductivity, which are all the influential factors for dielectric properties. Additionally, nickel-containing materials display antimicrobial activities through multiple mechanisms, including the creation of reactive oxygen species, the release of metal cations, and the disruption of microbial cell membranes, thus making nickel-containing materials desirable for biomedical applications.[18]

Based on the features of silicate-based systems such as higher mechanical stability, chemical durability, chemical stability, and promising electronic structures, advanced nanomaterials based on nickel (Ni^{2+})-doped magnesium aluminosilicate (Ni^{2+}-MAS) were investigated herein.[19,20] The integration of Ni^{2+} ions within the magnesium aluminosilicate glass-ceramic framework was designed to tailor the charge distribution, defect states, and bonding configuration, thereby enhancing the optical, dielectric, and antimicrobial functionalities.[21,22] This strategy allows the progress of multifunctional Ni^{2+}@MAS systems with enhanced performance for electronic, sensing, catalytic, and biomedical-related applications.

In this work, Ni^{2+}-doped magnesium aluminosilicate (MAS) glass-ceramic nanospheres were successfully synthesized *via* a controlled sol–gel route using a hydrolytic acid process, enabling low-temperature fabrication with improved physicochemical properties. The study systematically investigated the influence of Ni^{2+} incorporation (0–5 mol%) on the structural evolution, phase composition, and nanoscale morphology of MAS, and how these modifications govern the resulting multifunctional properties. Particular emphasis is placed on establishing the correlations between lattice distortion, defect formation, and surface characteristics with changes in electronic structure, optical band gap, dielectric response, and antimicrobial activity. The incorporation of Ni^{2+} is shown to alter the charge distribution and defect states within the MAS network, thereby affecting the phase purity and functional performance. Furthermore, a comparative evaluation of the antibacterial activity of pristine and Ni^{2+}-doped MAS nanospheres in powder form is presented. Overall, this work provides a comprehensive understanding of the composition-dependent structure–property relationships and highlights the potential of Ni-modified MAS nanoceramics for applications in functional ceramics and antimicrobial materials.

2 Experimental

2.1 Preparation of materials

The sol–gel precursor solutions of Ni^{2+}-doped magnesium aluminosilicate (Ni^{2+}@MAS) were prepared based on stoichiometric proportions, with the individual components added stepwise during the synthesis process.

The starting materials for the synthesis of Ni^{2+}@MAS nanoceramics included magnesium acetate (MgO), aluminum acetate (Al_2O_3), tetraethyl orthosilicate (SiO_2), ethanol (C_2H_5OH), hydrochloric acid (HCl), ethylenediamine (EDA), and nickel nitrate. Distilled water was added to facilitate hydrolysis. The chemical compositions of the Ni^{2+}@MAS samples, expressed in mol%, are as follows: MAS-0Ni (MgO 10, Al_2O_3 30, SiO_2 50, and NiO 0), MAS-1Ni (MgO 10, Al_2O_3 30, SiO_2 44, and NiO 1), MAS-3Ni (MgO 10, Al_2O_3 30, SiO_2 42, and NiO 3), and MAS-5Ni (MgO 10, Al_2O_3 30, SiO_2 40, and NiO 5), with all samples nucleated with 10 mol% SiO_2. Sol–gel glass-ceramic nanospheres were prepared with fixed $MgO : Al_2O_3$ ratios and varying SiO_2 contents, and doped with NiO at the specified concentrations.

Magnesium acetate and aluminum acetate were dissolved in 25 mL of deionized water before the addition of 10 mL of ethylenediamine (EDA), which served as a chelating ligand to control the metal ion coordination. Tetraethoxysilane (TEOS) was dissolved in 20 mL of absolute ethanol and hydrochloric acid (2 : 0.3) with 5 mL of EDA. Then, magnesium-aluminum solutions were added gradually to the TEOS solution under continuous vigorous stirring for 25 min.

For the Ni-codoped samples, nickel nitrate dissolved in a distilled water/ethanol/EDA mixture (2 : 1 : 1) was added dropwise to a magnesium silicate solution under vigorous stirring for 40 min, corresponding to Ni/magnesium silicate ratios of 1–5 mol% at room temperature. Subsequently, the Al_2O_3 solution was introduced into the Ni/magnesium silicate mixture and stirred vigorously for an additional 80 min. The obtained sols were aged for 20 h, dried at 70 °C for 15 h, and finally calcined at 700 °C at a heating rate of 5 °C min. Fig. 1 shows the preparation steps of Ni^{2+}@MAS glass-ceramic nanospheres.

2.2 Characterization

The Ni^{2+}@MAS glass-ceramic nanospheres were examined using X-ray diffraction (XRD; XPERT-X) analysis with Cu Kα radiation. The crystallite size was calculated using Scherrer's equation[23,24] as follows:

$$\left[D = \frac{K\lambda}{\beta \cos \theta_{hkl}}\right],$$

where K(constant) = 0.89, λ = 1.5405 Å (Cu Kα radiation), and β is the full width at half maximum intensity (I) of the peaks obtained from XRD.

The particle nature of the prepared samples was studied using transmission electron microscopy (TEM, Tecnai T20) analysis. The particle size distribution was estimated from TEM micrographs by digital image analysis using the ImageJ software. The images were calibrated using the scale bar provided in the micrographs, and individual particle diameters were measured manually.

The FTIR spectra of the prepared samples were recorded in the range of 4000–200 cm^{-1} using KBr pellets. For measuring the transmission and optical bandgap of Ni^{2+}@MAS glass-ceramic nanospheres, UV-vis-diffuse reflectance spectroscopy (JASCO V550) analysis was employed. The optical band gap values were calculated using the Tauc method based on the diffuse reflectance spectra transformed *via* the Kubelka–Munk function.[25,26]

2.3 Antibacterial assessment (agar diffusion assay)

The antimicrobial performance of the synthesized nanostructures (Ni(0), Ni (1), Ni (3), and Ni(5)) was evaluated against four pathogenic microorganisms using the agar well diffusion method.

The antibacterial activity was evaluated using a standardized agar diffusion protocol. Briefly, 20 mL of sterile nutrient agar medium (0.1% beef extract, 0.5% peptone, 0.2% yeast extract, and 0.5% NaCl; HiMedia Pvt. Ltd, India) was poured into Petri dishes and allowed to solidify under aseptic conditions at pH 7.4 ± 0.2. An aliquot (100 μL) of overnight bacterial suspension

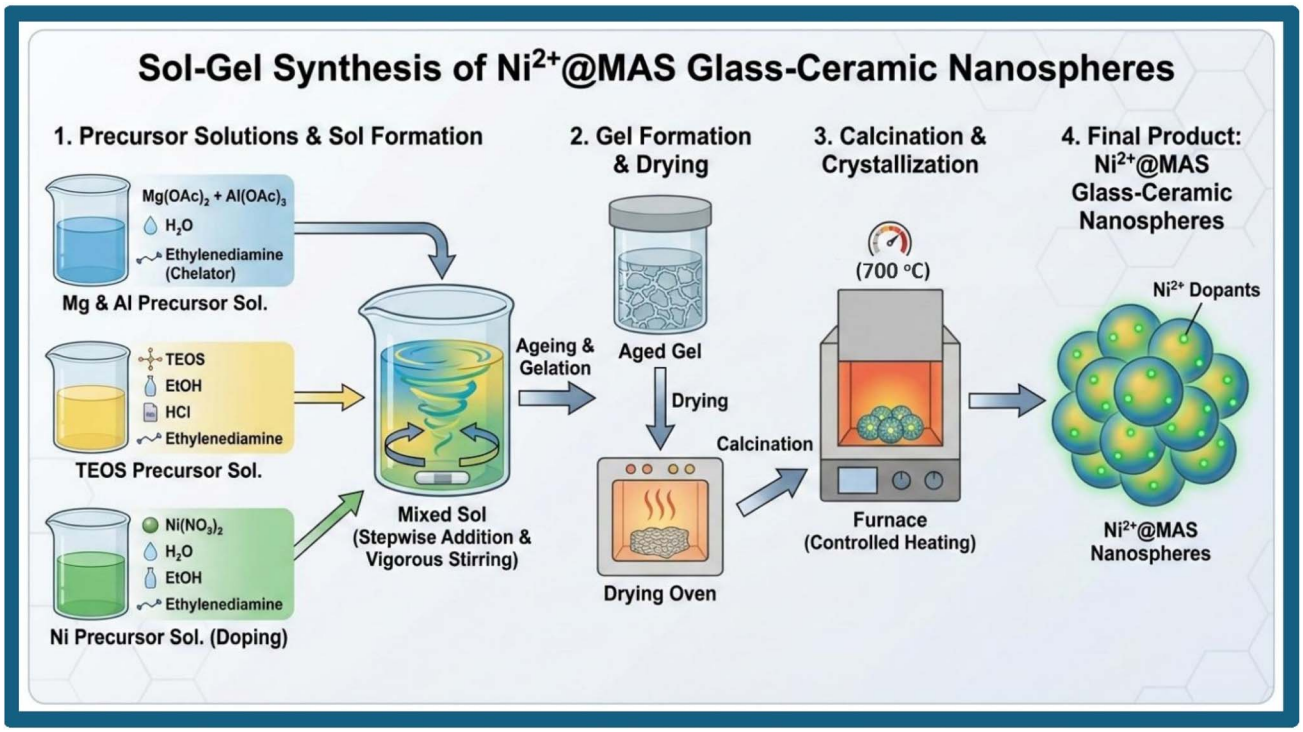

Fig. 1 Preparation steps of the Ni^{2+}@MAS glass-ceramic nanospheres.

($\sim 10^7$ CFU. mL^{-1}) was uniformly spread onto the agar surface using a sterile cotton swab.

The Ni@magnesium aluminosilicate samples were carefully placed onto the inoculated agar to ensure direct and uniform interfacial contact. The plates were incubated at 37 °C for 24 h. The inhibition zones formed around the samples were measured in millimeters, and the experiments were conducted in triplicate to ensure reproducibility.

Direct sample-agar contact was maintained to evaluate the contact-mediated antibacterial activity of the Ni-functionalized magnesium aluminosilicate system.

3 Results and discussion

3.1 Crystal structure and phase identification

The XRD pattern of Ni^{2+}-doped magnesium aluminosilicate is presented in Fig. 2. The XRD shows well-defined peaks, which refer to the polycrystalline nature of the composite samples. According to Fig. 2, the XRD of all samples shows a mixed composition, where the asterisk refers to the peak positions of the hexagonal $Mg_2Al_4Si_5O_{18}$ (PDF card 84-1600), while the middle dot refers to the position of the orthorhombic Mg_2SiO_4 (PDF card 89-7711-orthorhombic) and $Mg_{1.397}Ni_{0.599}SiO_4$ (PDF card 84-1983-orthorhombic). As observed in Fig. 2, the undoped sample MAS-0Ni shows that the intensity of hexagonal $Mg_2Al_4Si_5O_{18}$ peaks is the most dominant, which indicates that hexagonal $Mg_2Al_4Si_5O_{18}$ is the major phase, while the secondary phase is the orthorhombic Mg_2SiO_4 that has relatively low-intensity peaks.

Intensified orthorhombic peaks at $2\theta = 23.22°$, 25.8°, 29.8°, 30.2°, and 35.63° correlate with higher Ni contents, indicating that selective phase substitution is triggered by progressive Ni^{2+} doping.

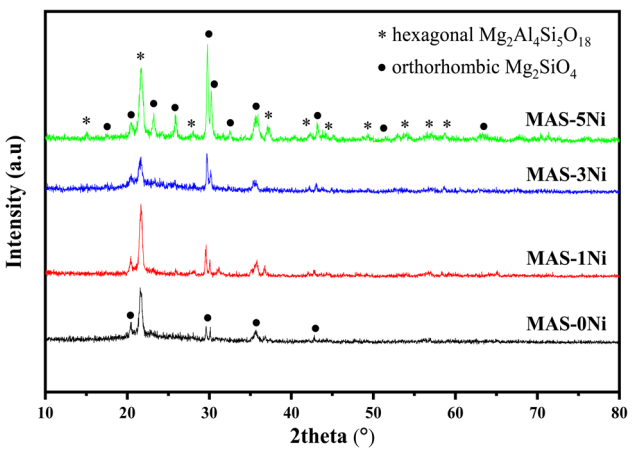

Fig. 2 X-ray diffraction (XRD) patterns of the pristine and Ni^{2+}-doped magnesium aluminosilicate (MAS) nanoceramics with different Ni contents (0–5 mol%). The diffraction peaks are indexed according to the corresponding crystalline phases, and the reference JCPDS card numbers are indicated. The absence/presence of secondary phases and peak shifts reflects the incorporation of Ni^{2+} into the MAS lattice and the resulting structural modifications.

The phase evolution of Ni^{2+}-doped MAS nanoceramics can be understood based on the substitution mechanism of Mg^{2+} by Ni^{2+} within the aluminosilicate lattice. Since both Mg^{2+} and Ni^{2+} possess the same valence state, the substitution is isovalent and does not require additional charge compensation. Moreover, the relatively comparable ionic radii of Mg^{2+} ($\sim$0.72 Å) and Ni^{2+} ($\sim$0.69 Å) favor the incorporation of Ni^{2+} into Mg^{2+} sites without significant lattice disruption. However, the slight difference in ionic size and electronic configuration leads to local lattice distortion and induces defect states within the glass-ceramic network. These structural perturbations are reflected in the observed peak shifts and variations in peak intensity in the XRD patterns, indicating changes in crystallinity and phase composition with the increase in Ni content. At higher Ni concentrations, the increased defect density and local strain may influence the phase stability and promote the formation of minor secondary phases or structural rearrangements. Overall, the Ni^{2+} substitution modifies the short- and medium-range order of the MAS network, which plays a crucial role in governing the observed optical, dielectric, and antimicrobial properties. The indexed peaks exactly match $Mg_{1.397}Ni_{0.599}SiO_4$ (PDF 84-1983), confirming the substitution.

The lattice parameters of the orthorhombic Mg_2SiO_4 were estimated using the following equation:

$$\frac{1}{d^2} = \frac{h^2}{a^2} + \frac{k^2}{b^2} + \frac{l^2}{c^2}.$$

The estimated lattice parameters and crystallite size are summarized in Table 1.

These distinctive reflections not only supported the incorporation of Ni^{2+} into the MAS glass-ceramic nanospheres but also recognized the good crystallinity of NiO inside the glass-ceramic nanospheres. Without altering the primary hexagonal phase positions, this solid solution formation improves the phase stability and crystallinity of Mg_2SiO_4, indicating that Ni incorporation happens by isomorphic substitution rather than secondary phase nucleation. Despite the altered surface basicity and porosity of these composite materials, such doping probably modifies lattice parameters, potentially improving the physicochemical features. The average of the crystallite sizes calculated using the Scherrer equation is 19.5, 23, 26, and 27 nm for (a) MAS-0Ni, (b) MAS-1Ni, (c) MAS-3Ni, and (d) MAS-5Ni nanoceramics, respectively (Table 1). The crystallite size was estimated using the Scherrer equation by fitting the most intense diffraction peaks using a pseudo-Voigt function, where the full width at half maximum (FWHM) values were extracted

Table 1 Estimated lattice parameters of the orthorhombic Mg_2SiO_4

Sample	a (Å)	b (Å)	c (Å)	Crystallite size (nm)
MAS-0Ni	4.808	10.171	5.925	19.5
MAS-1Ni	4.818	10.105	5.988	23
MAS-3Ni	4.889	10.2306	5.9215	26
MAS-5Ni	4.874	10.066	5.945	27

after baseline correction. The estimated uncertainty in crystallite size is ±1–2 nm, arising from peak fitting and instrumental limitations.

The XRD patterns of Ni^{2+}@MAS nanospheres proved that integrating Ni-ions leads to an obvious increase in crystallite size and improved peak intensity. This behavior indicates enhanced crystallinity and structural assembling with the higher Ni content. The increase in the crystallite size can be attributed to Ni^{2+} ions that promote lattice growth during the sol–gel mechanisms through facilitating nucleation and reducing structural defects, which can positively influence the material's optical, electrical, and antimicrobial properties.

3.2 TEM morphology and particle size analysis

The transmission electron microscopy (TEM) images of the calcined samples at 700 °C (MAS-0Ni and MAS-5Ni) are shown in Fig. 3a and b, respectively. Both samples exhibit a very similar physical structure to that of quasi-spherical primary ceramic nanospheres with branched, fractal-like aggregates normally observed in the aluminosilicate systems produced *via* sol–gel or precipitation methods, followed by high-temperature calcination.[27] For MAS-0Ni, the particle contrast was very uniform, indicating that aluminosilicate has a very uniform composition and does not contain any secondary phases of higher atomic number. Strong necking was exhibited by the particles, indicating that at the time of calcining at 700 °C, MAS-0Ni had begun to partially sinter. This explains why the magnesium aluminosilicates become viscous and coarse due to the onset of viscous flow and solid-state diffusion, as described previously.[27]

The morphology of MAS-5Ni is considered to be similar to that of the corresponding matrixes supporting the other phases; therefore, it is concluded that the incorporation of Ni(II) cations does not change significantly either how the host matrixes grow or the mechanism of aggregation. A slightly increased heterogeneity due to the presence of Ni(s) is observed in MAS-5Ni because of the differences in their respective electron densities. In addition, based on the results of conventional transmission electron microscopy, the presence of NiO or large

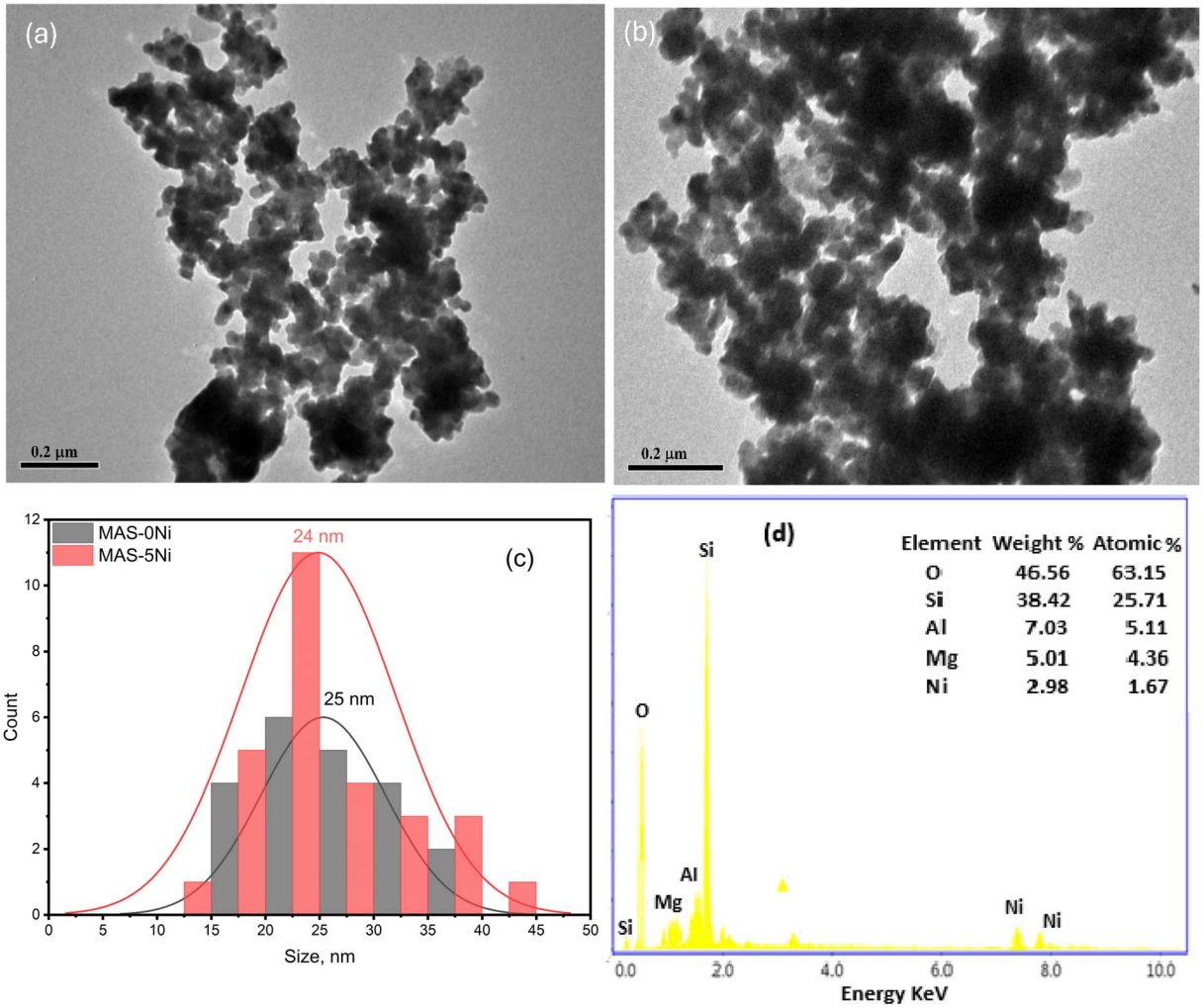

Fig. 3 TEM images of (a) MAS-0Ni and (b) MAS-5Ni. (c) Particle distribution plot and (d) EDX pattern of the MAS-Ni nanoceramics. Transmission electron microscopy (TEM) images of the Ni^{2+}-doped MAS nanoceramics show nearly spherical nanoparticles with a size distribution in the range of 20–30 nm.

crystalline NiO or aggregated NiO does not appear to have been detected in MAS-5Ni, which suggests that very little (if any) has been segregated from the host aluminosilicate matrix, and a very small amount may be incorporated into the amorphous or poorly crystalline aluminosilicate network. There are similar findings in previously published studies with transition metal-doped aluminosilicates, and those findings show that when dopants are present in the aluminosilicate framework, they replace Mg(II) or are located on distorted octahedral sites, with very little to no discernible diffraction from the oxide clusters.[28–30]

Fig. 3c shows the particle size distribution of both samples. The distribution shows that both samples have very similar size distributions with particle diameters falling predominantly in the range of 20–30 nm and that most of the particles from both samples had their mean particle diameter at 25 nm (MAS-0Ni) and 24 nm (MAS-5Ni). The fact that MAS-0Ni has a higher mean particle diameter than MAS-5Ni is not statistically significant, and is likely due to the experimental uncertainty associated with this type of quantitative analysis. However, the minor reduction in the mean particle size for the MAS-5Ni sample, when compared to the MAS-0Ni sample, is indicative of the inhibition of particle growth by Ni^{2+} doping during the calcination step. The mechanism by which this occurs has been explained in the literature as a result of the presence of Ni^{2+} ions increasing the concentration of defects, locally distorting the aluminosilicate network and producing a greater number of defect sites that inhibit the movement of mass and cause particle agglomeration during thermal processing.[31–34]

The size distribution of both materials is relatively narrow, indicating a consistent nucleation and growth process for both composites, whereas the presence of aggregates in both composites supports the existence of strong interparticle forces and partial sintering at 700 °C. The absence of a separate population of considerably larger amounts of MAS-5Ni also supports the interpretation that Ni^{2+} is distributed homogeneously rather than existing as separate Ng-rich crystallites, which would otherwise create an identifiable size fraction.[35,36] The EDX spectrum confirms the successful formation of a multicomponent MAS-Ni, as shown in Fig. 3(d). EDX analysis of these crystals confirms the typical forms of the crystalline structure MAS-Ni. The major peaks corresponding to O, Si, and Al verify the formation of the aluminosilicate framework, while the presence of Mg and Ni peaks indicates their effective incorporation within the MAS matrix. The relatively high O and Si contents validate the integrity of the silicate backbone, while the presence of Al, Mg, and Ni supports the formation of a modified MAS structure. Overall, the compositional distribution confirms the formation of a homogeneous MAS-Ni system with potential influence on dielectric and antimicrobial properties.

3.3 FTIR study

The FTIR spectra of Ni^{2+}-doped magnesium aluminosilicate (MAS) ceramic nanospheres (Fig. 4) verified in the range of 400–4000 cm^{-1} expose the main characteristic vibrational bands

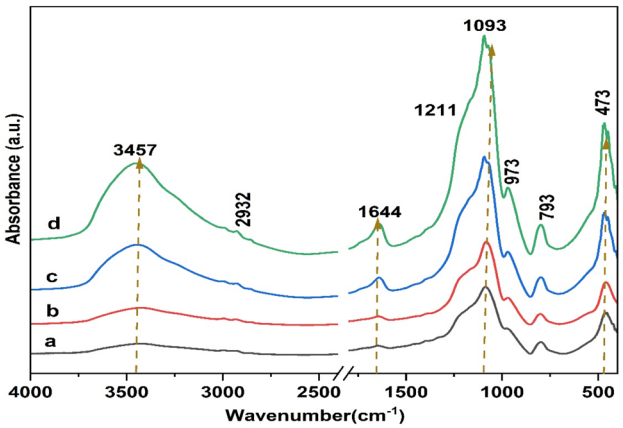

Fig. 4 FTIR spectra of the magnesium aluminosilicate ceramic nanospheres with different Ni^{2+} contents of (a) 0 Ni^{2+}, (b) 1 Ni^{2+}, (c) 3 Ni^{2+}, and (d) 5 Ni^{2+}.

related to silicate-based, hydroxyl groups and metal (Al, Mg, and Ni)–oxygen bonds, confirming the successful Ni^{2+} integration into the MAS framework.

The O–H stretching vibrations appear as a broad absorption band at 3457 cm^{-1} attributed to the surface hydroxyl groups and actually adsorbed water molecules. Moreover, the band at 1644 cm^{-1} is ascribed to the –OH bending vibration of adsorbed water molecules representing the hydrophilic surface characteristics of the aluminosilicate matrix.[37,38]

The increase in intensity with Ni^{2+}-doping proposes improved surface hydroxylation and increased defect density, encouraged by Ni^{2+} incorporation. The observed changes in O–H stretching and bending vibrations in the spectra of undoped MAS and Ni^{2+}-doped samples were within the expected range.[39,40] These changes can be attributed to OH absorption and structural modifications occurring during the polycondensation process, which become more pronounced with increasing Ni^{2+} content due to its incorporation into the MAS network through oxygen bonding.

The weak absorption band observed at 2932 cm^{-1} is attributed to the –CH stretching vibrations, which are associated with the adsorbed atmospheric contaminants or residual organic species. The presence and strengthening of the shoulder at 1211 cm^{-1} may be due to Si–O–Si, Si–O–Mg, Si–O–Al and Si–O–Ni asymmetric stretching vibrations.[38,41] This authorizes that a well-advanced MAS-based network has formed. The intensity development in MAS after Ni^{2+} doping indicates the alteration of the silicate-based tetrahedral units and stouter network connectivity.

The main absorption peak near 1093 cm^{-1} is typical for the Si–O–Si bonds. This stronger peak originates from the asymmetric stretching vibrations, which supports the dominant structural feature of the MAS-based material. The intensity increases noticeably with the increase in Ni^{2+} doping, indicating structural modification and partial substitution of Mg^{2+}/Al^{3+} sites by Ni^{2+} ions within the MAS network.[37,41] The absorption band 973 cm^{-1} is assigned to Si–O–M (M = Mg, Al and Ni) stretching vibrations, confirming Ni^{2+} incorporation into the

MAS lattice. The peaks observed at 793 cm^{-1} and 473 cm^{-1} correspond to the symmetric stretching of Si–O–metal bonds and metal–oxygen (Al–O, Mg–O, and Ni–O) vibrations, further confirming the integrity of Mg, Al, and Ni in the silicate network. The increase in the intensity of these peaks provides strong evidence for the successful incorporation of Ni^{2+} ions into the MAS lattice rather than forming separate NiO phases, also showing altered local bonding environments due to the Ni–O–Si interactions.[42] Moreover, the chemical band at 793 cm^{-1} could be attributed to the formation of the aluminosilicate ring structure (SiO_4 tetrahedra and [AlO_4]-tetrahedron) of the Si–O–Al bond.[43,44]

Generally, systematic shifts in the main vibrational peaks were noted with the increase in Ni contents. The (Si–O–Si) asymmetric stretching vibration at 1081 cm^{-1} for MAS-0Ni displayed a progressive red shift from 1081 cm^{-1} (MAS-0Ni) to 1093 cm^{-1} (MAS-5Ni), matching a shift value of ~12 cm^{-1}. Similarly, the –OH stretching band shifted from ~3447 to 3457 cm^{-1} ($\Delta\nu \approx 10$ cm^{-1}). These shifts exceed instrumental uncertainty, confirming that the observed changes arise from Ni^{2+}-induced bond weakening and lattice distortion within the MAS network.

3.4 Optical diffuse reflectance properties

Fig. 5a shows the diffuse reflectance (DR) spectra of magnesium aluminosilicate glass-ceramic samples doped with various amounts of Ni^{2+} ions (0, 1, 3 and 5 mol%) heat-treated at 700 °C. The reflectivity patterns show how the refractive index of the glass-ceramic changed structurally and electronically when nickel was incorporated into the host matrix. The MAS-0Ni sample has a very high level of reflectance through the entire visible spectrum, while it has a very well-defined absorption edge in the UV region (<300 nm) and multiple structural overtones in the near-infrared region, indicating that it is an insulator due to the presence of a silicate-based host structure. Once nickel is added, distinct decreased areas in reflectance (associated with light absorption) develop, and their intensity is proportional to the amount of Ni^{2+} added. The MAS-5Ni sample has the clearest features in the spectrum and displays three areas of depressed reflectance intensity at about 433 nm, 828 nm, and a broad band above 1200 nm. These areas correspond to the d–d electronic transitions of Ni^{2+} ions ($3d^8$ configuration) in octahedral coordination (O_h symmetry), substituting for Mg^{2+} or Al^{3+} ions within the nano-crystal spinel ($MgAl_2O_4$) that were produced during a calcination step at 700 °C.[45]

The pronounced dip in reflectance in the blue-violet region at 433 nm is assigned to the transition from the ground state ($^3A_{2g}(F)$) to the excited state ($^3T_{1g}(P)$) (ν_3). The second broad dip, centered around 828 nm, corresponds to the transition from the ground state ($^3A_{2g}(F)$) to the excited state ($^3T_{1g}(F)$) transition (ν_2), and the broad feature observed in the near-infrared region at 1200 nm is attributed to the lower energy transition from the ground state ($^3A_{2g}(F)$) to the excited state ($^3T_{2g}(F)$) (ν_1).[46] The pronounced high reflectance in the region from 500 to 700 nm, peaking at about 650 nm in the MAS-5Ni sample, indicates a "window of transmission" in the green-orange region of the light spectrum; because of the very high transmission properties, a greenish or yellowish color is produced on the ceramic phase in which the octahedral Ni species dominate as opposed to the tetrahedral Ni species, which would exhibit strong absorption in the visible red region of the light spectrum.[47] In addition, a rapid reduction in reflectance below 350 nm for each sample indicates that all samples are undergoing the optical band gap transition that is required for the charge to transfer from the O^{2-}(2p) orbitals to the metal cation valence bands.[48]

Fig. 5b depicts the optical absorbance spectra for the MAS glass-ceramic system containing 0, 1, 3, and 5 mol% Ni^{2+} ions, all calcined at 700 °C, and demonstrating the development of optical features in accordance with the concentration of the

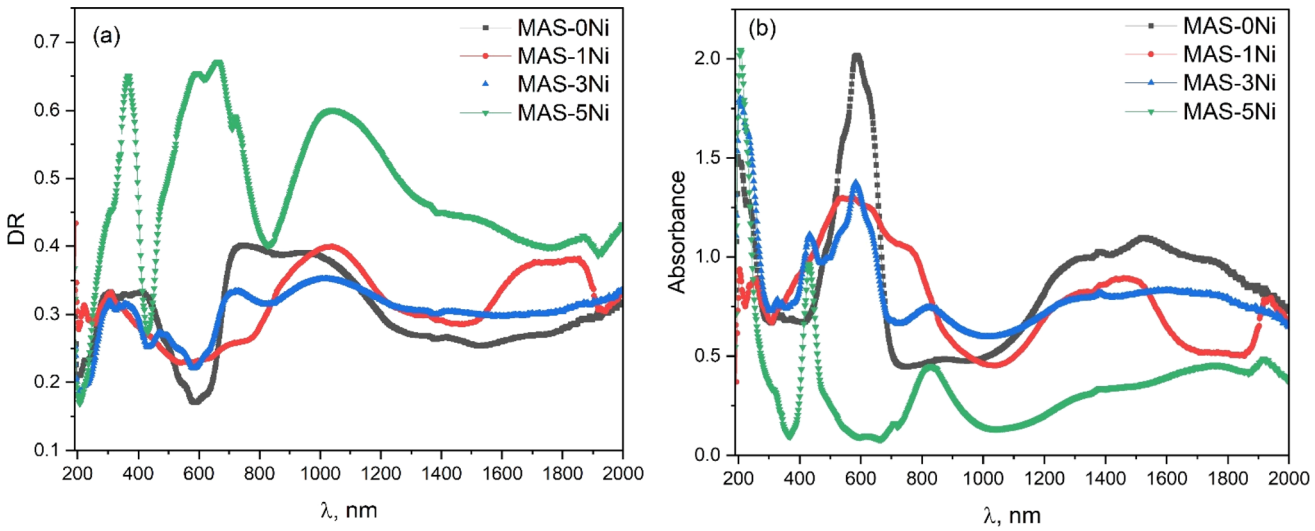

Fig. 5 (a) Diffuse reflectance spectra and (b) corresponding absorbance spectra of the pristine and Ni^{2+}-doped magnesium aluminosilicate (MAS) nanoceramics with Ni contents of 3 and 5 mol%, calcined at 700 °C. The variation in spectral features with the increase in Ni^{2+} concentration reflects the changes in the optical absorption behavior associated with modifications in the electronic structure of the MAS matrix.

nickel dopant. This change in optical properties is indicative of the different coordination environments and electronic structures created by the addition of nickel, as well as the evolution of optical properties due to the density of the nickel ions.[49]

The MAS-0Ni sample does not contain any nickel, showing that there are broadbands with high intensity throughout the visible spectrum at about 400 nm. The high level of opacity in the visible range appears to have been caused by light scattering due to the heterogeneous nature of the glass-ceramic microstructure, as well as the presence of defects remaining in the host matrix as a result of calcining the sample at 700 °C prior to the development of the fully stabilized optical phase.[50]

The spectra have become more characteristic of metal oxides with the addition of nickel, which resulted in the appearance of characteristic bands that became more distinct as the amount of nickel in the sample was increased (MAS-3Ni and MAS-5Ni). The MAS-5Ni sample, which contains the most distinct spectral features, is characterized by three strong absorption bands present in the spectral region of 366 nm, 650 nm, and 1045 nm. The three absorption bands represent the signature or fingerprint of Ni^{2+} ions in the $3d^8$ electronic state that occupy octahedral coordination sites of the structure (O_h).[51]

According to the ligand field theory (LFT) for a d^8 ion in an octahedral field, these bands correspond to the three spin-allowed electronic transitions from the ground state $^3A_{2g}(F)$ to the excited states:[52–54] (i) the sharp absorption band in the violet region (366 nm) is assigned to the $^3A_{2g}(F)$-to-$^3T_{1g}(P)$ transition (ν_3). (ii) The broad band centered in the near-infrared region (650 nm) corresponds to the $^3A_{2g}(F)$-to-$^3T_{1g}(F)$ transition (ν_2). (iii) The absorption rising in the longer wavelength region (1045 nm) is attributed to the lowest energy $^3A_{2g}(F)$-to-$^3T_{2g}(F)$ transition (ν_1).

A significant "transparency window" (minimum absorption) around 433 nm is found in the sample containing MAS-5Ni. Due to this transparency window being located at 433 nm, it accounts for the characteristic green color that is typically observed in nickel-doped spinel ceramic materials, which indicate that Ni^{2+} ions preferentially occupy the octahedral site of the precipitating $MgAl_2O_4$ nanocrystals as opposed to the tetrahedral site, where they would produce strong absorption in the red/visible region of the spectrum and provide a blue color instead of green.[52] Furthermore, the gradual appearance of these bands as the Ni concentration increases from MAS-1Ni to MAS-5Ni indicates that the increased nickel content in spinel ceramics promotes the stabilization of the nickel-spinel phase, therefore rendering them with optical quality and transparency in the green region of the spectrum.[53]

The values of the optical band gap were estimated *via* the Tauc method applied to diffuse reflectance data through the Kubelka–Munk relation.[25] The absorption coefficient was approximated using the Kubelka–Munk function $F(R)$, which is proportional to the absorption coefficient for optically thick samples. The band gap was extracted by plotting $(F(R)h\nu)^n$ as a function of photon energy ($h\nu$), where $n = 1/2$ and $n = 2$ correspond to direct and indirect allowed transitions, respectively.[25] The band gap energy was obtained by extrapolating the linear portion of the Tauc plot in the high-absorption region near the fundamental absorption edge to the photon energy axis ($h\nu$) where $(F(R)h\nu)^n = 0$. The linear fitting range was selected from the region exhibiting the best linear correlation above the absorption edge while avoiding low-energy tail states associated with defect-related absorption.[26] The same fitting procedure was applied consistently to all samples to ensure reliable comparison of the extracted band gap values.

Fig. 6a and b show Tauc plots of direct and indirect cases, respectively. The extracted band gap values are illustrated in Fig. 6c. The optical band gap behavior demonstrates systematic and non-linear transitions both directly and indirectly, as Ni is added to the MAS-Ni series. Both curves display a U-shaped trend, with the lowest band gap at MAS-1Ni, followed by an increase in both direct and indirect band gaps at MAS-3Ni and MAS-5Ni. This indicates that as Ni is incorporated into the electronic structure, the electronic gap becomes smaller initially, but then expands again with additional substitutions of Ni.

From a scientific perspective, these non-linear trends can be explained by the competing forces of dopant incorporation, lattice distortion, and alterations in the electronic structure.[55,56] When Ni is substituted in a lattice, localized defect states or perturbed band edges are produced, which initially bring states closer to each other, thus reducing E_g for the MAS-1Ni composition.[55,56] Numerous examples of dopant-induced band gap variation have been observed in transition metal-doped oxides and semiconductors, in which the introduction of in-band or band-edge states modifies optical transitions occurring in the electronic structure of the material.[55–59] For instance, in Ni-doped ZnO and similar systems, reports indicate that the introduction of Ni 3d states into the gap region produces a tailing effect on the absorption edge, thus decreasing the measured optical band gap compared to the host lattice without Ni.[55,56]

The optical band gap also increases with higher concentrations of Ni in MAS-3Ni and MAS-5Ni, possibly due to defects containing band-filling effects or simply due to increased carrier density at higher Ni concentrations. This behavior is often referred to as the Burstein–Moss effect,[60] when high concentrations of a dopant in a conductive oxide cause the additional carriers to occupy lower conduction band states, thus causing a shift of the apparent absorption edge to higher energies.[61,62] However, the definitive nature of confirming the Burstein–Moss effect usually requires the Hall effect measurements of carrier concentrations, which were not taken in this glass-ceramic system. As a result, we consider the Burstein–Moss effect as a possibility. Therefore, the band gap increase observed for higher Ni concentrations is more likely due to the combination of defect impurity band modification, lattice distortions, and electronic interactions associated with the dopant in question, which are common in transition metal-doped oxide materials.[63–65]

3.5 Dielectric study

3.5.1 Dielectric permittivity (ε'). The dielectric permittivity (ε') of Ni-doped MAS samples *vs.* frequency and at different temperatures (30 °C, 60 °C, and 100 °C) is presented in Fig. 7.

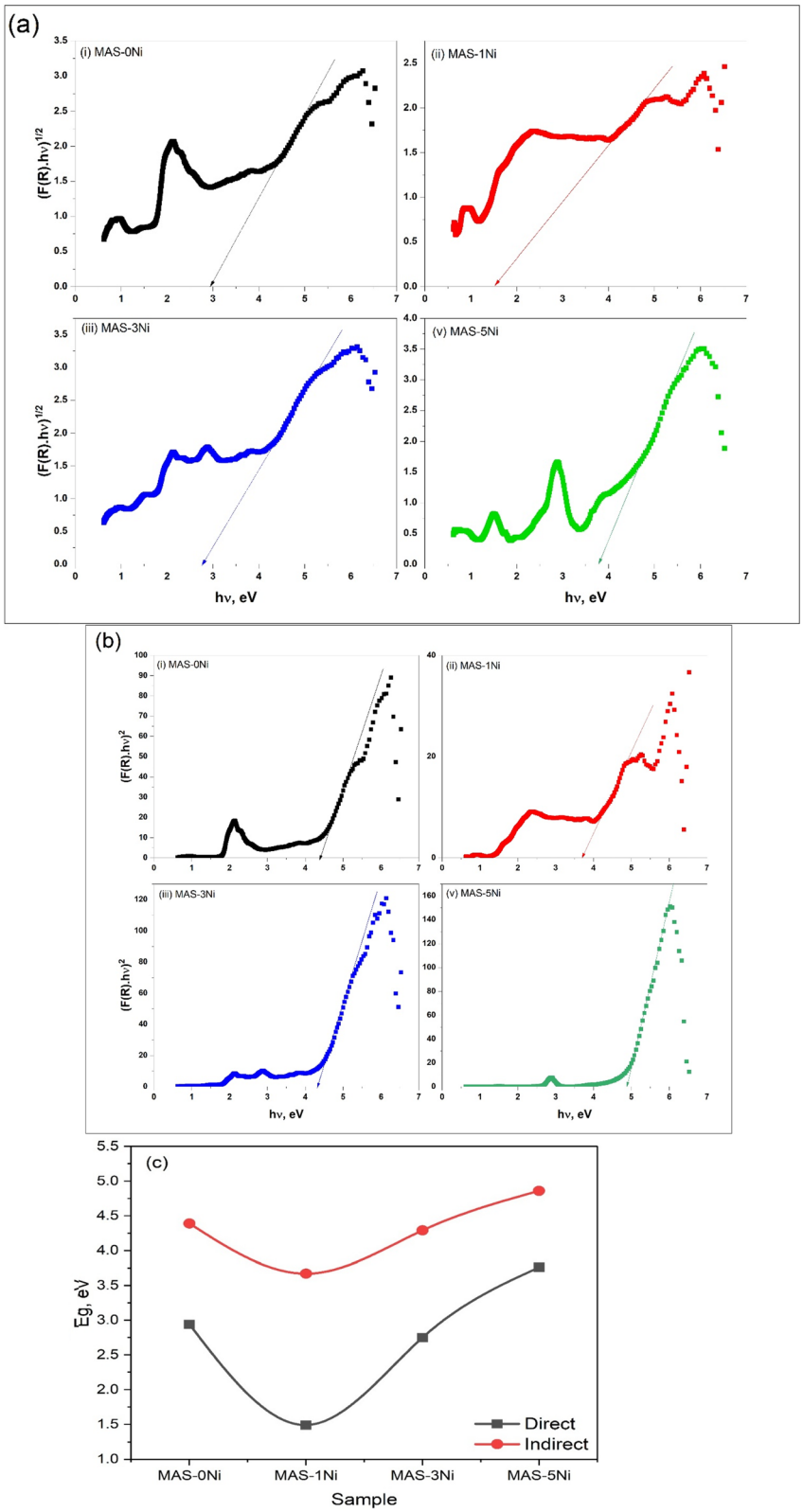

Fig. 6 Tauc plots for (a) direct allowed transitions and (b) indirect allowed transitions of the Ni^{2+}-doped magnesium aluminosilicate (MAS) nanoceramics with Ni contents of 3 and 5 mol%, calcined at 700 °C. The linear fitting regions used for band gap determination are indicated. (c) Variation in the optical band gap energy as a function of Ni^{2+} concentration, demonstrating the influence of Ni incorporation on the electronic structure of the MAS matrix.

The permittivity of MAS-0Ni (Fig. 7a) shows two flattened plateaus separated by a frequency dispersion that spans from 0.1 to 10 kHz. The first plateau spans from 0.1 to 100 Hz, while the second plateau lies at high frequencies from about 32 kHz to 8 MHz. The first plateau shows more stability and barely changes compared with that at higher frequencies, which shows relative dipping with the increase in frequency but with a small value of about 2. The first plateau lies at ~600 (at 30 °C) and shifts with heating to ~812 (at 60 °C) and to ~936 (at 100 °C). The onset point also shifts to higher frequencies with heating. The second plateau lies at ~20 (at 30 °C) and shifts with heating to ~17.5 (at 60 °C) and to ~15 (at 100 °C). The sample MAS-1Ni (Fig. 7b) shows enhanced permittivity values and low-frequency dispersion only below 1 Hz. The first plateau lies at ~153, ~253, and ~347 (with heating), while the permittivity reaches ~51 200 at 0.1 Hz and 100 °C. The first plateau shrinks as part of it represents low-frequency dispersion, while the high-frequency plateau extends from ~1 kHz to 8 MHz and sits at ~20 for all temperatures.

The mid-frequency dispersion strength and span are reduced. The sample MAS-3Ni (Fig. 7c) combines some features from the previous samples. Its first plateau lies at ~367, ~439, and ~645 (with heating), while the frequency dispersion spans from about 10 Hz to 1 kHz, and the high-frequency plateau covers the rest of the frequency range with values of ~17, ~19, and ~20 (at 30 °C, 60 °C, and 100 °C, respectively). The sample MAS-5Ni (Fig. 7d) shows similar behavior, but has the smallest values at 30 °C and 60 °C, while at 100 °C, it shows the highest values in the low-frequency region. The high-frequency plateaus nearly converge for MAS-1Ni and MAS-3Ni, while they look separated for MAS-0Ni and MAS-5Ni.

The different frequency regimes' behavior indicates multiple processes, such as interfacial effects along with some intrinsic lattice responses. The high-frequency plateau (~15–20) for most samples can be interpreted as intrinsic permittivity that originates from both electronic and ionic polarizations. The low-frequency plateaus are larger and strongly depend on both temperature and Ni-content, pointing to interfacial MWS or polarization.[66–68] MWS polarization occurs from the build-up of charges at the interfaces, such as grains, or grain boundaries, or at electrodes.[69,70]

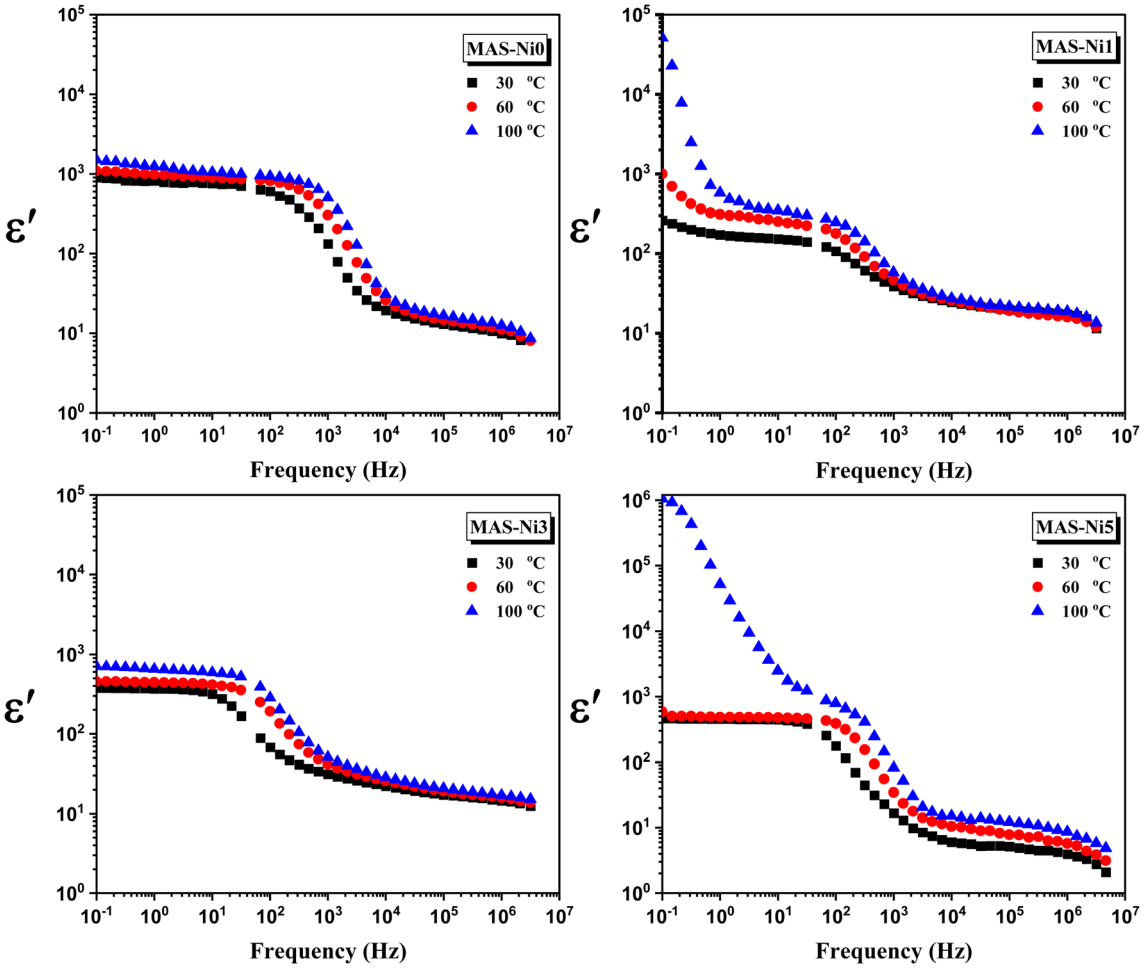

Fig. 7 Frequency dependence plots of the dielectric permittivity (ε′) of Ni^{2+}-doped magnesium aluminosilicate (MAS) nanoceramics with different Ni concentrations, measured over a range of temperatures. The observed dispersion in ε′ at low frequencies and its temperature dependence is attributed to interfacial (Maxwell–Wagner) polarization and space charge effects influenced by Ni^{2+} incorporation.

At low frequencies, the charges can follow the field variations, build up, and saturate at the interfaces. The charges cannot keep building up due to some limitations such as mobile charge concentration, interface area, and available time. Therefore, with the decrease in frequency, when a saturation is reached, ε' becomes frequency-independent and flattening occurs, while at higher frequencies, the interfacial charges cannot keep up with the field alternation, and again ε' becomes frequency-independent. The dispersion appears in the transition region where the system moves from incomplete charge build-up (at higher frequencies) to developed interfacial polarization (at lower frequencies). The flatness of the plateau depends on several factors such as relaxation time distribution, grain boundary thickness, and resistivity. A narrow distribution might result in a flatter plateau, while a broad distribution might develop a sloped or smeared plateau. The plateau observed at low frequencies is related to the MWS process (extrinsic capacitance), while that at higher frequencies is related to electronic and ionic polarizations (intrinsic capacitance).

Increasing the temperature thermally activates and increases charge mobility or concentration, which results in faster saturation, and then the relaxation frequency shifts to a higher frequency with heating.[71] The plateau height increases because more charges can build up at interfaces. The dispersion is seen at mid-frequencies, which could be owing to transitions from resistive to capacitive behavior.

The dramatic permittivity increment at low frequency (51 200 at 0.1 Hz, 100 °C for MAS-Ni1) is not intrinsic. It is dominated by space charge accumulation and conductivity contributions along interfaces and grain boundaries. This indicates that most polarization develops only at low frequencies where charges have sufficient time to build up at interfaces. In MAS-1Ni, the dominant low-frequency process is shifted to longer relaxation times, so most polarization develops only at low frequencies (<1 Hz) rather than forming a broad low-frequency plateau within the usual window; as a result, the apparent first plateau observed above ~1 Hz is lower than that in MAS-0Ni, while ε' rises sharply only when the frequency is reduced enough, where the charges have sufficient time to build up at interfaces, producing a very large apparent permittivity dominated by space-charge and conductivity contributions rather than intrinsic polarization. The very large ε' at 0.1 Hz is consistent with the formation of conductive paths or enhanced hopping conduction. The shrinkage of the first plateau and the extension of the high-frequency plateau indicate the overlapping of relaxation or conduction processes and reduced mid-frequency dipolar contribution. MAS-3Ni shows the intermediate behavior of combining features of MAS-0Ni and MAS-1Ni, indicating likely mixed contributions from grain dipoles and grain-boundary interfacial polarization.

MAS-3Ni shows intermediate behavior because Ni at this level modifies both the bulk and interfacial responses, and hence, both dipolar polarization inside grains and grain-boundary Maxwell–Wagner interfacial polarization are active. The sample exhibits moderate low-frequency values, slight mid-frequency dispersion, and a stable high-frequency plateau, suggesting no dominant contribution from either intrinsic grain polarization or charge accumulation and conductivity effects (as in MAS-1Ni). This intermediate response corresponds to moderate permittivity at low frequencies, arising from a balance between intrinsic and interfacial polarization. In contrast, MAS-5Ni exhibits anomalous behavior, with the lowest permittivity at low frequencies at 30 °C and 60 °C, which increases to the highest value at 100 °C. This behavior reflects stronger temperature dependence and increased charge trapping at low temperatures. At high temperatures, thermal activation frees carriers, leading to large low-frequency permittivity dominated by space charge and conductivity contributions. The high Ni content increases the defect density and localization of carriers, slowing relaxation. At low Ni content (1–3%), interfacial charge accumulation is enhanced without forming continuous conductive paths. For MAS-Ni5, the low-frequency permittivity shows strong temperature dependence. At high temperatures, thermal activation frees trapped carriers, leading to large low-frequency permittivity dominated by space charge and conductivity contributions. The high Ni content increases the defect density and localization of carriers, slowing relaxation and masking intrinsic polarization.

The dielectric behavior correlates with the structural and spectroscopic data. The host hexagonal phase provides the stable intrinsic polarizability that appears as a similar high-frequency plateau across samples. The changes in low-frequency permittivity follow the evolution of new phases and defects seen in different analyses. XRD shows an increased orthorhombic Ni-substituted phase with a higher Ni content. This raises the number of phase boundaries and enhances the conductivity difference between grains and grain boundaries.[72] This phase mismatch increases MWS and creates slower interfacial relaxation times. Thus, samples with larger orthorhombic fractions are expected to show stronger and more temperature-sensitive low-frequency responses. TEM shows a similar particle size with no large Ni clusters. This correlates with similar high-frequency permittivity values. At the same time, the microstructure heterogeneity causes some samples to show flat low-frequency plateaus, while others show smeared dispersion. When most interfaces have similar resistance and capacitance, their relaxation times are close, so the response appears as a flat low-frequency plateau. When the interfaces are different in thickness or conductivity, a wide range of relaxation times exist. This spreads the interfacial response over a broad frequency range, which appears as smeared or broadened dispersion instead of a clear plateau. FTIR spectroscopy analysis reveals stronger OH bonds and growing Si–O–Ni features with Ni doping. Increased surface hydroxylation and Ni–O–Si linkages provide more trap sites and surface conduction pathways. This enhances low-frequency permittivity and its temperature dependence.

The intrinsic dielectric permittivity comes from the stable host lattice, as indicated by TEM and FTIR spectroscopy analyses. The low-frequency response is controlled by extrinsic effects related to phase differences seen in XRD, defects and OH groups detected by FTIR spectroscopy and in-gap electronic states from the optical data. Together, these results show that Ni substitution introduces defects and hopping paths, which

enhance interfacial polarization and make the dielectric behavior strongly dependent on the Ni content and temperature.

3.5.2 Imaginary permittivity (ε''). The imaginary permittivity (ε'') for the sample *vs.* frequency and at different temperatures (30 °C, 60 °C, and 100 °C) is presented in Fig. 8. The imaginary permittivity decreases with the increase in frequency for all samples and temperatures. At low frequencies, ε'' has high values; these values increase with heating in all samples. The lowest-frequency region shows the largest separation between temperatures. At high frequencies, all curves approach small values close to unity or less. At low frequencies, ε'' rises sharply with the decrease in frequency, especially at high temperatures, and the slope is steep and nearly linear. This rise is strongest at 100 °C for all samples. At 100 °C, MAS-Ni1 and MAS-Ni5 show the highest low-frequency ε'' values. MAS-Ni0 and MAS-Ni3 show lower ε'' values. At 30 °C, MAS-Ni3 and MAS-Ni5 show the lowest ε'' values. At mid-frequencies, ε'' shows a broad peak or a feature of the relaxation process. The peak position shifts slightly to higher frequencies with temperature and shifts to lower frequencies with composition. The sample MAS-Ni5 shows an additional feature at high frequencies centered around 0.1 MHz. Any possible relaxation in the low-frequency region in samples MAS-Ni1 and MAS-Ni5 is masked by the linear fall corresponding to conductivity contributions.

The peak height increases with temperature. MAS-Ni0 shows a clear and broad peak centered at ~835 Hz at 30 °C that moves with heating to ~1018 and 1669 Hz at 60 °C and 100 °C, respectively. The MAS-Ni1 peak appears at 228 Hz at 60 °C and shifts to 342 Hz at 60 °C, and then the peak is masked by the linear behavior at 100 °C. The MAS-Ni3 peak is centered at ~41, ~116, and ~137 Hz at 30 °C, 60 °C, and 100 °C, respectively. The MAS-Ni5 peak appears at 157 Hz at 30 °C and shifts to 332 Hz at 60 °C, and then the peak is masked by the linear behavior at 100 °C as in MAS-Ni1.

Dielectric loss comes from interfaces and from charge motion. The low-frequency ε' and large ε'' are associated with interfacial/MWS polarization and charge transport, while the mid-frequency features originate from dipolar or interfacial relaxations with distributed times.[66] The high-frequency plateau of ε' comes from intrinsic polarizations that yield low loss. An increase in temperature enhances both charge carrier mobility and hopping rates, shifting the loss peaks toward higher frequencies and increasing their magnitude. The large low-frequency permittivity (*e.g.*, 51 200 at 0.1 Hz, and 100 °C for MAS-1Ni) is accompanied by huge dielectric loss with a linear downfall, which indicates great charge transport contribution.

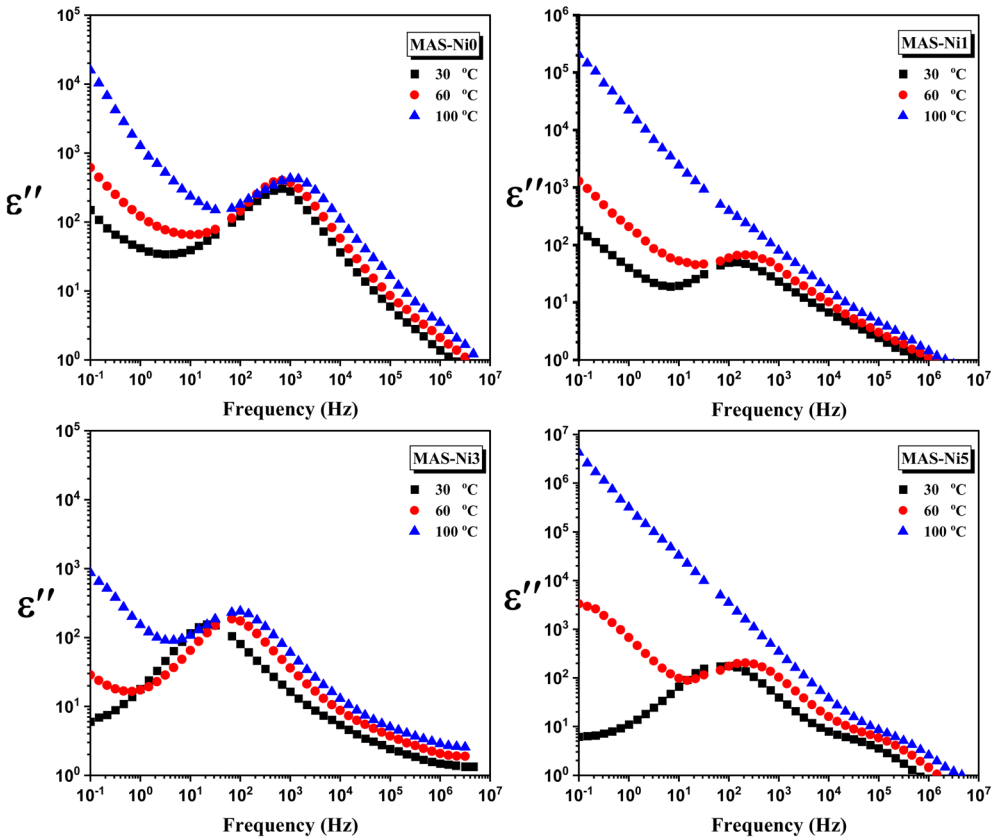

Fig. 8 Frequency dependence plots of the imaginary permittivity (ε'') for MAS-Ni0, MAS-Ni1, MAS-Ni3, and MAS-Ni5 measured at 30 °C, 60 °C, and 100 °C. The mid-frequency relaxation peaks shift to higher frequencies with the increase in temperature, indicating thermally activated relaxation. The steep low-frequency rise at 100 °C in MAS-Ni1 and MAS-Ni5 reflects conductivity-dominated loss. The high-frequency region shows low intrinsic loss for all compositions.

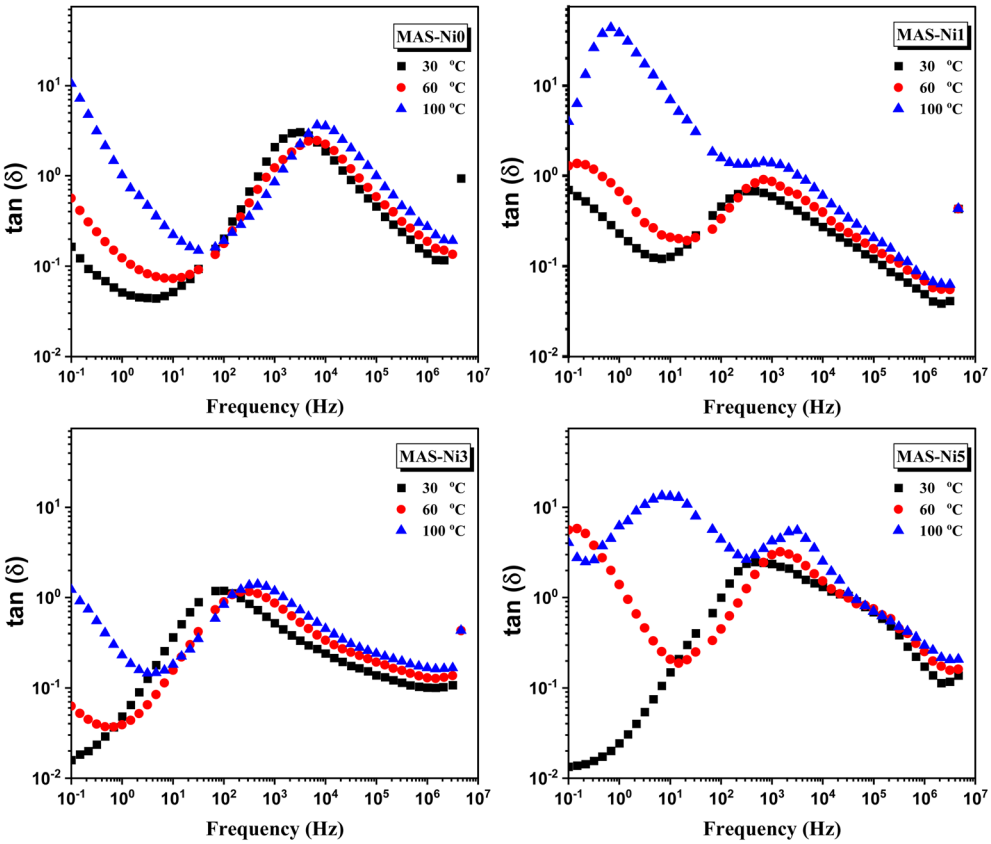

Fig. 9 Frequency dependence plots of dielectric loss tangent (tan δ) for MAS-Ni0, MAS-Ni1, MAS-Ni3, and MAS-Ni5 measured at 30 °C, 60 °C, and 100 °C. tan δ decreases with frequency for all samples, transitioning from conduction-dominated loss at low frequencies to intrinsic lattice loss at high frequencies. Additional low-frequency features in MAS-Ni1 and MAS-Ni5 near 0.7 Hz and 10 Hz correspond to conductivity-related relaxation. MAS-Ni3 maintains tan δ below 1 across the entire frequency and temperature range.

The noticed peaks or relaxation features correlate and coincide with the frequency dispersion observed in the permittivity curves. The low ε' and ε'' values at high frequencies, and the near temperature independence, indicate an intrinsic lattice response only. The broadness of the mid-frequency peak indicates a broad distribution of relaxation times, with non-Debye behavior.[73] The peak shifting to a higher frequency with temperature indicates thermally activated relaxation, while the high-temperature peak masking in MAS-1Ni and MAS-5Ni indicates overlap with the conduction contribution process.

The relaxation processes become activated with heating, as charges and dipoles gain energy and move faster, unlike at lower temperatures when their movement is slower. Thermal energy frees trapped carriers, and hence, increases their mobility hopping rates. Shorter relaxation times mean that the peaks move to higher frequencies. The peak shifts with the composition because Ni addition introduces defects and oxygen vacancies that change the local charge dynamics. The increased defects modify relaxation behavior by introducing carrier trapping and localized states. At a low Ni content, interfacial polarization is enhanced without forming continuous conductive paths. At a higher Ni content, the higher defect density and localized carriers mask intrinsic relaxation peaks and lead to stronger temperature-dependent low-frequency permittivity. The peak position depends on the dominant response. Capacitive polarization leads to peaks at lower frequencies due to longer relaxation times, while increasing the conductivity shortens the relaxation time and shifts the peak to higher frequencies or masks it. More grain boundaries and phase interfaces increase interfacial loss at a low frequency. Defects and oxygen vacancies enhance charge carrier hopping, which leads to an increase in both the dielectric loss (ε'') and the loss tangent (tan δ). The decreased grain size and the heterogeneous structure broaden the loss peaks and increase dispersion. A higher Ni content means more connected conductive regions that increase the low-frequency loss and mask relaxation peaks, especially at high temperatures, while more uniform and dense structures show lower and more stable loss.

3.5.3 Dielectric loss tangent (tan δ). The loss tangent decreases with frequency for all samples and temperatures (Fig. 9). The same relaxation features observed in the dielectric loss are present in the loss tangent, along with others at low frequency in MAS-Ni1 and MAS-Ni5, which correspond to the conductivity contribution relaxation. These new features are centered at ~0.7 Hz and at ~10 Hz in MAS-Ni1 and MAS-Ni5. It is high at low frequencies and low at high frequencies. Low-frequency tan δ increases with temperature. MAS-Ni1 and MAS-Ni5 show tan δ values larger than 1 at low frequencies,

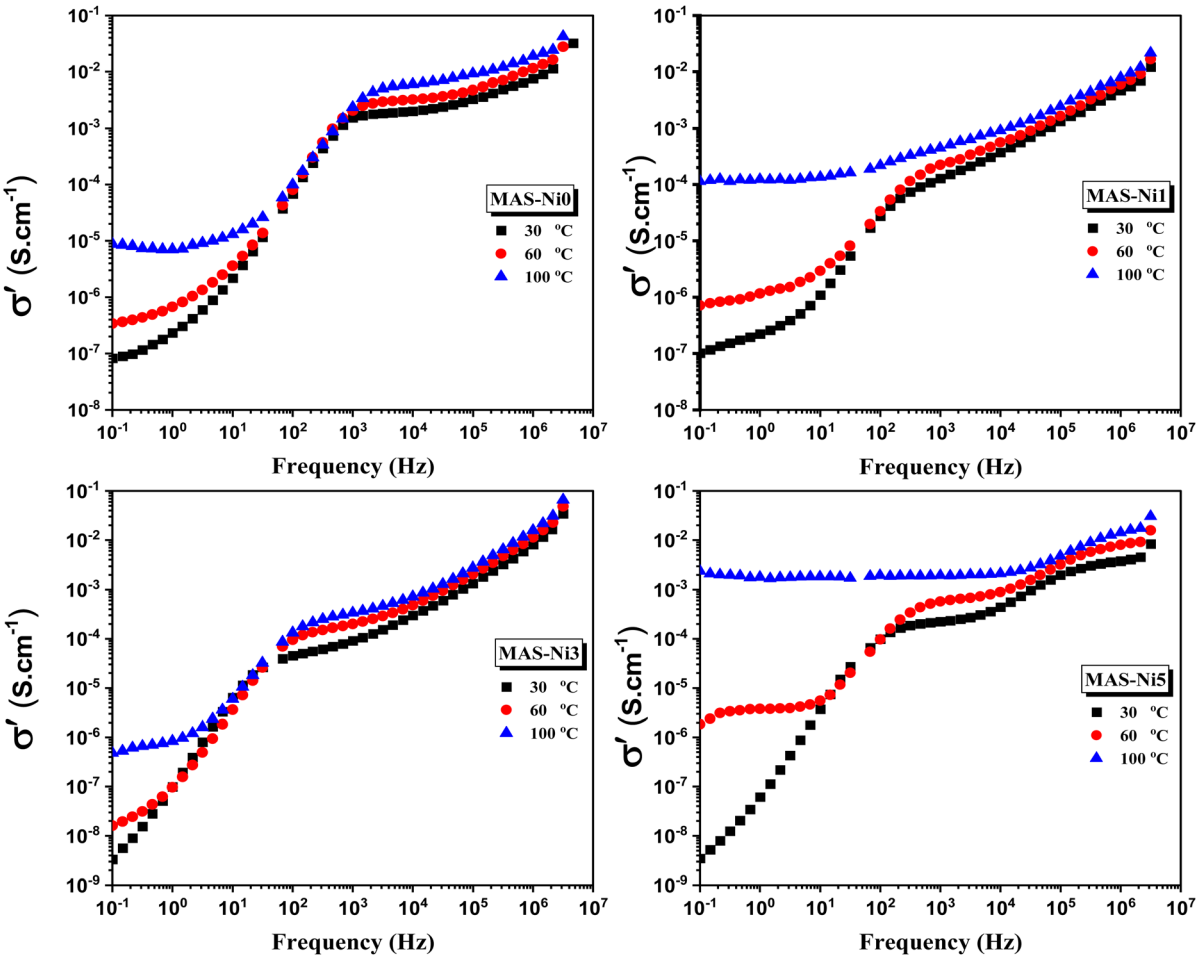

Fig. 10 Frequency dependence of AC conductivity (σ') for MAS-Ni0, MAS-Ni1, MAS-Ni3, and MAS-Ni5 measured at 30 °C, 60 °C, and 100 °C. Three regions are identified: a low-frequency DC plateau arising from long-range charge transport, a dispersive mid-frequency region following the power law corresponding to short-range hopping, and a high-frequency semi-plateau reflecting lattice-limited hopping. MAS-Ni5 shows the largest temperature-dependent conductivity variation, spanning from 10^{-9} S cm^{-1} at 30 °C to above 10^{-3} S cm^{-1} at 100 °C.

especially at high temperatures. MAS-Ni3 keeps tan δ below 1 over the whole frequency and temperature range. At high frequencies above about 1 MHz, tan δ drops to small values around 0.01–0.1 and shows little temperature dependence.

The decrease in tan δ with frequency shows the change from conduction-controlled loss at a low frequency to intrinsic loss at a high frequency. The extra low-frequency features in MAS-Ni1 and MAS-Ni5 near 0.7 Hz and 10 Hz are linked to conductivity-related relaxation, which is enhanced by higher defect density, grain-boundary contrast, and possible conductive paths formed with a higher Ni content. The rise in low-frequency tan δ with temperature comes from thermally activated charge motion along interfaces and defects. MAS-Ni3 keeps tan δ below 1 because its structure provides a balanced grain and grain-boundary response with fewer connected conductive paths. At high frequencies, where tan δ is small and nearly temperature independent, the response is mainly controlled by the stable host lattice and is weakly affected by microstructural variations.

Due to the strong contribution of conductivity at low frequencies, relaxation analysis was performed using the loss tangent (tan δ), which provides clearer peak definition. The high-frequency relaxation peaks shift toward a higher frequency with the increase in temperature, indicating thermally activated relaxation. The peak frequency (f_{max}) was used to estimate the activation energy using Arrhenius behavior.[66] The extracted activation energies are 0.13 ± 0.04 eV for MAS-Ni0, 0.14 ± 0.03 eV for MAS-Ni1, 0.23 ± 0.07 eV for MAS-Ni3, and 0.25 ± 0.05 eV for MAS-Ni5. The increase in activation energy with the Ni content indicates progressively stronger localization of charge carriers and slower relaxation. Slight deviation due to overlapping processes is expected, especially for MAS-Ni3 and MAS-Ni5.

3.5.4 AC conductivity (σ'). The AC conductivity increases with frequency and temperature for all samples (Fig. 10), and it is characterized by 3 regions. In the low-frequency range (0.1 to ~1 Hz), the curves are flatter, which represents DC conductivity arising from the long-range motion of charges through the grains causing interfacial build-up at grain boundaries. As the frequency rises, the conductivity starts to increase quickly for all samples, following the power law.[66] The charges can no longer move long distances with a smaller time allowed since the field

switches become faster. The charges then hop between neighboring sites. At frequencies above 1 kHz, the conductivity continues to rise, but the rate of increase slows down significantly. This region reflects short-range hopping within the lattice. The frequency is so high that the contribution from moving charges is limited by the physical structure of the lattice. This creates a semi-plateau, even though the values are still slowly climbing.

Conductivity increases with temperature and reaches higher values at elevated temperatures. The increment in temperature is better observed at low frequencies, while the temperature separation effect between curves is less effective at higher frequencies. High temperatures provide more energy for charge carriers and the charges can hop in a longer range, which extend the conductivity plateau. The amount of nickel in the MAS-Ni samples changes the conductivity levels, which reflects the changes in defect density and local charge dynamics. MAS-Ni0 starts with a low-frequency conductivity near 10^{-7} S cm^{-1} at 30 °C. MAS-Ni5 shows a much wider change with temperature. At 30 °C, MAS-Ni5 has the lowest conductivity at 10^{-9} S cm^{-1}, but at 100 °C, it shows a very high and flat plateau at nearly above 10^{-3} S cm^{-1}. MAS-Ni1 and MAS-Ni3 show intermediate values between these two extremes. The introduced defects seem to be activated only by temperature, as it seems to block the motion of charges and decrease the conductivity at low temperatures. The charges are trapped at lower temperatures, but thermal energy at 100 °C frees them to move across these defects. This leads to a sharp rise in conductivity and a clearer low frequency dc region. This conduction behavior is consistent with the Arrhenius analysis of tan δ peak frequencies, where E_a increases with the Ni content.

The AC conductivity values demonstrated in this work span from 10^{-9} S cm^{-1} at low temperatures for MAS-Ni5 to above 10^{-3} S cm^{-1} at 100 °C, covering a range relevant to several functional applications. The stable low conductivity at room temperature combined with thermally activated response makes these materials suitable candidates for temperature-sensitive switching elements and thermal sensors operating in the intermediate frequency range. The frequency window studied, from 0.1 Hz to 8 MHz, covers the range used in impedance-based humidity and gas sensors, where the frequency-dependent conductivity plateau and dispersion region provide sensitive detection parameters. The high-frequency intrinsic permittivity of 15–20, stable across all compositions and temperatures, is consistent with requirements for substrate materials in microwave and RF passive components. The tunability of both conductivity and dielectric response through the Ni^{2+} content provides an additional design parameter for optimizing these materials toward specific application requirements.

3.5.5. Cole–Cole analysis and correlation with structural and electrical properties. The Cole–Cole plots (ε'' *vs.* ε') were constructed for all compositions at 30 °C, 60 °C, and 100 °C and are shown in Fig. 11. These plots are used to separate intrinsic dielectric relaxation from extrinsic electrode polarization contributions, and to connect the dielectric response to the structural and electrical properties already discussed. At 30 °C and 60 °C, all four samples show a single depressed semicircular arc. A perfectly circular arc would indicate a single relaxation time, which is the ideal Debye behavior. The depression observed here means that a distribution of relaxation times is present, which is the expected behavior for polycrystalline ceramics with structural heterogeneity. The degree of arc depression increases progressively from MAS-Ni0 to MAS-Ni5. This is consistent with the XRD results, which show that increasing the Ni content introduces a growing orthorhombic $Mg_{1.397}Ni_{0.599}SiO_4$ phase alongside the dominant hexagonal $Mg_2Al_4Si_5O_{18}$ phase. The coexistence of two phases with different polarizabilities and conductivities creates a wider variety of interface types and local environments, which broadens the distribution of relaxation times and deepens the arc depression. The FTIR results support this, showing that Si–O–Ni bonds and surface hydroxyl groups increase with Ni content, adding further trap sites and local heterogeneity. The activation energies extracted from the tan δ Arrhenius analysis, which increase from 0.13 eV for MAS-Ni0 to 0.25 eV for MAS-Ni5, are consistent with this picture. Higher activation energy means more localized carriers and slower, more distributed relaxation, which is precisely what a more depressed arc represents in the Cole–Cole plot.

The diameter of the semicircular arc at 30 °C reflects the total intrinsic polarization strength of the material. The arc diameter is largest for MAS-Ni0 and changes non-linearly across the series, with MAS-Ni1 showing a relatively large arc despite its lower Ni content. This is consistent with the optical band gap results, which show a minimum band gap at MAS-Ni1 due to localized defect states introduced by the initial Ni substitution. A narrower band gap means more accessible electronic states, which increases the polarization strength and is reflected in the larger arc diameter at this composition. The TEM results show that all samples consist of quasi-spherical nanospheres with strong necking between particles. This necking creates resistive constrictions at grain contacts, which increases the grain boundary resistance and shapes the Cole–Cole arc. The similar particle morphology across samples explains why the basic arc shape is consistent across all compositions, while the compositional differences account for the changes in arc size and depression.

At 100 °C, all four samples show a near-vertical rise of ε'' at comparatively low ε' values. This behavior is the signature of electrode polarization caused by space-charge accumulation at the sample–electrode interface. The full-scale insets confirm that ε'' reaches approximately 1.6×10^4, 2×10^5, and 5×10^8 for MAS-Ni0, MAS-Ni1, and MAS-Ni5, respectively, at 100 °C. The severity of this divergence follows the same order as the AC conductivity values reported in Section 3.5.4. MAS-Ni5 shows the most extreme electrode polarization and also the largest conductivity jump, from 10^{-9} S cm^{-1} at 30 °C to above 10^{-3} S cm^{-1} at 100 °C. MAS-Ni0 shows the smallest electrode polarization artifact and also the most stable conductivity across temperatures. This direct correspondence confirms that the electrode polarization is driven by thermally activated charge transport rather than intrinsic polarization. When conductivity rises sharply at 100 °C, mobile charges reach the

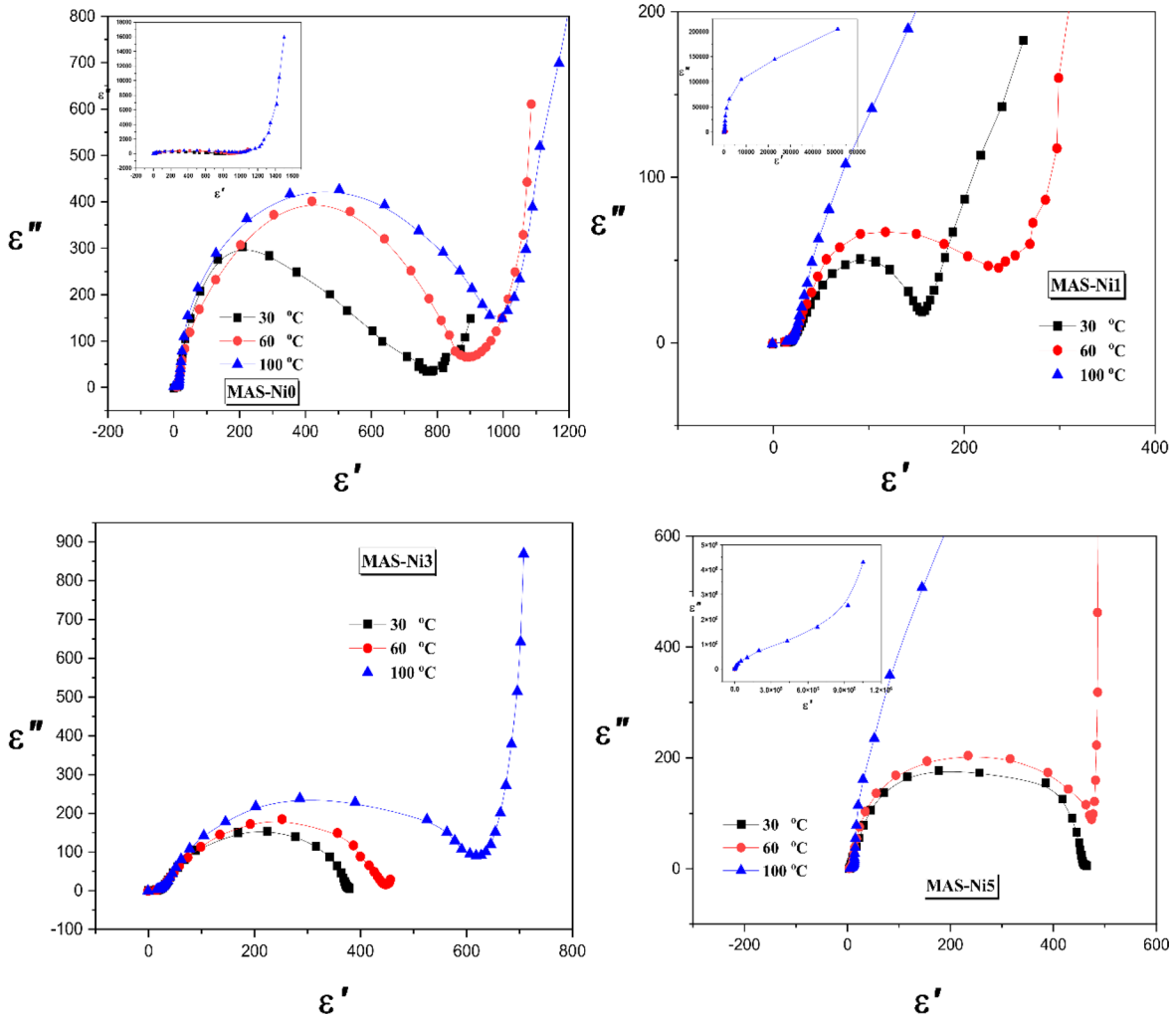

Fig. 11 Cole–Cole plots (ε'' *vs.* ε') for MAS-Ni0, MAS-Ni1, MAS-Ni3, and MAS-Ni5 measured at 30 °C, 60 °C, and 100 °C. Insets in MAS-Ni0, MAS-Ni1, and MAS-Ni5 show the corresponding full-scale plots at 100 °C. The full-scale 100 °C divergence for MAS-Ni3 is visible within the main plot scale. All samples show single depressed semicircular arcs at 30 °C and 60 °C representing intrinsic non-Debye dielectric relaxation. At 100 °C, a near-vertical divergence of ε'' confirms electrode polarization dominance at low frequencies.

electrode interface faster and accumulate more extensively, producing the large ε'' divergence seen in the Cole–Cole insets. This is fully consistent with the Maxwell–Wagner–Sillars mechanism described in Section 3.5.1, where charge build-up at interfaces governs the low-frequency dielectric response.

At 30 °C and 60 °C, where electrode polarization is absent, the Cole–Cole arcs represent genuine material relaxation, and reliable dielectric parameters can be extracted from them. At 100 °C, the electrode polarization completely dominates the low-frequency response for all samples. This confirms that the anomalously large low-frequency permittivity values reported at elevated temperatures, including the value of 51 200 at 0.1 Hz for MAS-Ni1 at 100 °C, are extrinsic in origin and reflect space-charge accumulation rather than intrinsic material properties. The high-frequency permittivity values of 15 to 20, which are stable across all compositions and temperatures, represent the true intrinsic response of the material arising from electronic and ionic polarization within the lattice.

The structural and dielectric results together establish a consistent mechanistic picture. Ni^{2+} substitution into the MAS lattice proceeds by replacing Mg^{2+} sites in the orthorhombic Mg_2SiO_4 phase, as confirmed by XRD. This substitution progressively increases the orthorhombic phase fraction alongside the dominant hexagonal phase. The two coexisting phases are expected to have different polarizabilities and conductivities, increasing the conductivity contrast across grain and grain-boundary interfaces. A higher conductivity contrast is consistent with stronger Maxwell–Wagner–Sillars interfacial polarization, which accounts for the increasing low-frequency permittivity with the Ni content. At the same time, Ni substitution introduces oxygen vacancies and localized defect states, as confirmed by FTIR spectroscopy through growing Si–O–Ni bonds and increased surface hydroxylation. These defects act as carrier trapping sites, which increases the distribution of relaxation times. This broader distribution is reflected by the progressive deepening of the Cole–Cole arc depression from

MAS-Ni0 to MAS-Ni5. The Arrhenius activation energies of 0.13, 0.14, 0.23, and 0.25 eV for MAS-Ni0 through MAS-Ni5 quantify this progressive carrier localization. At low temperatures, carriers remain trapped at these defect sites, which limits conductivity and keeps the low-frequency permittivity moderate. At 100 °C, thermal energy releases trapped carriers, conductivity rises sharply, and space-charge accumulates at the electrode interface, producing the electrode polarization confirmed by the Cole–Cole divergence. This sequence, from Ni substitution to phase boundary formation to interfacial polarization to electrode polarization at high temperatures, is consistent at each step, as indicated by XRD, FTIR spectroscopy, Cole–Cole analysis, conductivity, and activation energy data in this work.

3.6 Antimicrobial activity

The antimicrobial behavior of Ni^{2+}@ magnesium aluminosilicate samples (Ni(0)–Ni(3)) prepared *via* the sol–gel process was evaluated against representative Gram-positive bacteria (*Bacillus cereus* and *Staphylococcus aureus*), Gram-negative bacteria (*Escherichia coli* and *Helicobacter pylori*), and pathogenic yeast (*Candida albicans*), through the agar well diffusion technique. The inhibition zone diameters obviously indicate that all prepared Ni^{2+}@MAS@ samples display good antimicrobial activity, with performance strongly dependent on Ni^{2+} content. The results verified an inhibitory effect that varied with the contents of Ni. At a nanoparticle concentration of 75.0 μl, inhibition zone diameters of 19.0 ± 0.4 mm, 11.0 ± 0.5 mm, 16.0 ± 0.4 mm, 18.0 ± 0.4 mm, 18.0 ± 0.4 mm, and 11.0 ± 0.4 mm were observed for *Staphylococcus aureus*, *Bacillus cereus*, *Escherichia coli*, *Helicobacter pylori*, and *Candida albicans*, respectively. Increasing the contents of Ni^{2+} in MAS improved the inhibition zones given in Table 2. The reduced susceptibility of *Helicobacter pylori* and *Staphylococcus aureus* is likely due to the formation of stronger Ni–O–Mg/Si/Al bonds, which immobilize Ni species within the aluminosilicate matrix and restrict the controlled release of bioactive Ni^{2+} ions.[74,75]

The presence of activated Ni-ions, often in combination with Mg, Al, and SiO_2, produces an effective antibacterial agent promising for bio-related applications like bone substitutes and bone generations.[75] Mainly, the continuous release of active Ni^{2+} ions, the direct interactions between nanoparticles and cell membranes and the production of reactive oxygen species (ROS), all of which cause membrane damage and cellular entry, exert antibacterial effects.[76,77] The MAS-based system helps spread out the nanoparticles and preserves the active sites steadily, which makes the antibacterial action stronger.

Additionally, Al_2O_3, MgO, and NiO phases formed in MAS@Ni^{2+} offer high chemical stability, confirming durability under harsh conditions and higher suitability for biomedical and environmental applications.[78] Magnesium oxide (MgO) nanoparticles exhibit notable antimicrobial activity, increased toxicity toward bacteria, and antioxidant properties. The primary mechanisms involve the generation of reactive oxygen species (ROS), disruption of biological membranes, and inhibition of biofilm formation. Studies have demonstrated that MgO nanoparticles effectively inhibit the growth of both Gram-positive and Gram-negative bacteria, as well as unicellular fungi and yeasts, at different concentrations (0.5 to 1.6 mg mL^{-1}).[78,79]

Gajendiran *et al.* studied the antibacterial properties of (MgO/NiO) nanocomposites.[80] Their study confirmed pronounced antibacterial activities against both *S. aureus* and *E. coli*; this improved efficacy was attributed to the increased oxygen vacancies and surface defects, which induce reactive oxygen species generation and higher interactions with the bacterial cell membranes.[80,81] NiO nanoparticles have revealed effective antimicrobial potential against various strains including *Micrococcus luteus*, *E. coli*, *Klebsiella pneumoniae*, *Streptococcus mutans*, *Salmonella typhi*, and *Bacillus cereus*.[80,82] Their antimicrobial outcome is ascribed to both oxidative stress from metal ion release and the non-oxidative reactions (physical-membrane mutilation and disruption of permeability). Hence, increasing the NiO_2 content enhances the ability of MAS to combat various microbiological strains.[83] The observed antimicrobial effects demonstrate that Ni^{2+}@MAS glass-ceramic nanospheres exhibit significant and dose-dependent antimicrobial activity, highlighting their promise for antimicrobial coatings and biomedical applications.

Finally, the enhanced antimicrobial activity of Ni^{2+}-doped magnesium aluminosilicate nanoceramics is likely driven by a synergistic mechanism involving surface interactions, possible Ni^{2+} ion release, and oxidative stress effects. The nanoceramic surfaces can electrostatically interact with negatively charged bacterial membranes, leading to membrane destabilization and increased permeability, which facilitate further antimicrobial processes. Gradual release of Ni^{2+} ions may penetrate microbial cells and disrupt essential intracellular functions, while transition metal centers can promote the formation of reactive oxygen species (ROS), inducing oxidative damage to lipids, proteins, and DNA. The observed increase in antimicrobial efficiency with the increase in Ni content suggests a composition-dependent effect, potentially linked to the changes in surface chemistry and defect density. It should be noted that this proposed mechanism is inferred from experimental trends and literature reports.[84,85]

Ni^{2+}-doped magnesium aluminosilicate nanoceramics show superior antimicrobial properties against the tested microbes compared to previously studied materials. However, previously studied magnesium aluminosilicate (MAS) in its undoped form was not associated with significant intrinsic antimicrobial activity; however, its high surface area, adsorption capacity, and

Table 2 Inhibition zone diameter (millimeter) of the samples determined by applying the well diffusion method

	Test bacteria				
Samples	*Escherichia coli*	*Helicobacter pylori*	*Bacillus cereus*	*Staphylococcus aureus*	*Candida albicans*
Ni (0)	16.0	18.0	11.0	19.0	11.0
Ni (1)	18.0	13.0	11.0	18.0	14.0
Ni (2)	19.0	15.0	12.0	21.0	14.0
Ni (3)	16.0	13.0	12.0	16.0	13.0
** CN**	15.0	20.0	20.0	18.0	19.0

ion-exchange capability make it an excellent host matrix for antimicrobial enhancement through metal ion incorporation.[85] Previous studies on aluminosilicate systems, particularly zeolite-based materials, have demonstrated that metal-ion doping markedly improves the antimicrobial performance.[86] For instance, silver-loaded aluminosilicates exhibit significantly enhanced bacterial inhibition compared to free silver ions, as evidenced by larger inhibition zones, indicating a synergistic role of the matrix in controlled ion delivery and microbial interaction.[85,86] Similarly, Ag/MgO co-doped zeolitic systems show superior antimicrobial efficiency due to the combined effects of Ag^{+} ion release and MgO-induced reactive oxygen species (ROS) generation, leading to strong dose-dependent bacterial inhibition.[85,86] Other transition metal dopants, such as Cu and Zn, have also been reported to enhance the antimicrobial activity in aluminosilicate and ceramic systems, with effectiveness depending on factors such as dopant concentration, oxidation state, and distribution within the matrix.[84,87] These improvements are generally attributed to multifaceted mechanisms, including sustained metal ion release, oxidative stress induced by ROS, and surface-mediated disruption of microbial cell membranes.[85–87] Therefore, compared to undoped MAS, metal ion-doped MAS systems exhibit significantly enhanced antimicrobial activity, highlighting the critical role of dopants in tailoring biological functionalities while also potentially improving additional properties such as adsorption and drug delivery capabilities.

Since dielectric permittivity depends on crystal structure, defect formation, bonding characteristics, and microstructural homogeneity, its variation is effectively correlated with results obtained from different characterization techniques such as XRD, FTIR, SEM, and TEM. The observed enhancement in low-frequency permittivity is interpreted in terms of Maxwell–Wagner–Sillars (MWS) interfacial polarization and defect-assisted charge transport, which are well-established mechanisms in heterogeneous ceramic systems. The improved antimicrobial performance with the increasing Ni content is attributed to the combined effects, including possible Ni^{2+} ion release, reactive oxygen species (ROS) generation, and surface interaction with microbial membranes, consistent with widely reported mechanisms for transition metal oxide systems. The observed variations in dielectric and antimicrobial properties are strongly correlated with the structural evolution of the system, including phase composition, crystallite size, and local bonding environment, highlighting a clear structure–property relationship in Ni^{2+}-doped MAS nanoceramics. We acknowledge that these interpretations are indirect and phenomenological, as no direct measurements of charge carrier dynamics, ion release kinetics, or ROS generation were performed.

4 Conclusion

Ni^{2+}-doped magnesium aluminosilicate (MAS) nanoceramics were successfully synthesized *via* a low-temperature sol–gel route, demonstrating controlled structural evolution with the varying Ni content. The main advantage of this work lies in establishing a clear correlation between Ni^{2+} incorporation, defect formation, and the resulting multifunctional properties. Ni doping effectively tailors the electronic structure, leading to tunable optical band gaps, enhanced dielectric response, and improved AC conductivity through defect-mediated charge transport. Furthermore, the incorporation of Ni^{2+} significantly enhances the antimicrobial activity, highlighting the dual-functional capability of these materials. The combination of low-temperature synthesis, tunable physicochemical properties, and enhanced antimicrobial performance positions Ni-modified MAS nanoceramics as promising candidates for advanced functional ceramics, dielectric devices, and antimicrobial applications.

The presence of Ni doping has little impact on particle morphology, but it does have some effects on the amount of particle growth during calcination. The optical analysis confirmed the presence of Ni^{2+} ions in octahedral coordination, producing a green transparent window characteristic of nickel-spinel structures. The decrease in band gap at low concentrations of Ni and the increase with higher ones are due to the competition of defects and band filling effects. Thus, Ni doping is a viable way to modify the optical characteristics of MAS glass-ceramics. Ni^{2+} substitution progressively increases the phase boundary density, strengthening Maxwell–Wagner–Sillars interfacial polarization and broadening the relaxation time distribution, confirmed by Cole–Cole arc depression and activation energies increasing from 0.13 to 0.25 eV. At elevated temperatures, thermally released carriers produce electrode polarization that dominates the low-frequency response, while the intrinsic permittivity remains stable at 15–20 across all compositions. These results demonstrate that the Ni^{2+} content provides a controllable parameter for tuning the dielectric response of MAS glass-ceramics across a wide range and that the Cole–Cole analysis reliably separates intrinsic contributions from extrinsic contributions, enabling the accurate characterization of the true material. The antimicrobial activity of the Ni^{2+}@MAS glass-ceramic nanospheres was found to be induced by integrating Ni-ions and is more potent against *Escherichia coli* and *Staphylococcus* species in a composition-dependent manner. This behavior arises from the metal-ion release, ROS generation, and framework disruption mechanisms, supported by stable $MgO–Al_2O_3–SiO_2$ phases. These findings confirm that Ni^{2+}@MAS nanoceramics are promising candidates for opto-electronic devices, photonic devices, bone-regenerative scaffolds, antimicrobial ceramic membranes, and biomedical applications.

Author contributions

This work was done through the contributions of all authors. All authors have approved this final version of the manuscript.

Conflicts of interest

The authors declare that they have no known competing financial interests or personal relationships that could have appeared to influence the work reported in this paper.

Data availability

The datasets used and/or analyzed during the current study are available from the corresponding author upon reasonable request.

Acknowledgements

This work was supported and funded by the Deanship of Scientific Research at Imam Mohammad Ibn Saud Islamic University (IMSIU) (grant number IMSIU-DDRSP2602).

References

1 K. O. Shvydyuk, J. Nunes-Pereira, F. F. Rodrigues and A. P. Silva, *Ceramics*, 2023, **6**, 195–230.
2 M. A. Gatou, E. Skylla, P. Dourou, N. Pippa, M. Gazouli, N. Lagopati and E. A. Pavlatou, *Crystals*, 2024, **14**, 215.
3 M. Khan, G. A. Nowsherwan, R. Ali, M. Ahmed, N. Anwar, S. Riaz, A. Farooq, S. S. Hussain, S. Naseem and J. R. Choi, *Molecules*, 2023, **28**, 7963.
4 Y. Wang, Y. Peng, W. Qin, L. Zhu, Y. Xie, B. Liu, X. Wang, G. Zhang and D. Xu, *J. Eur. Ceram. Soc.*, 2026, **46**, 118128.
5 L. Wang, S. Li, Z. Zhang, Y. Guo, J. Cao and X. Xia, *Ceram. Int.*, 2026, **52**, 1530–1551.
6 B. Yan, Z. Chen, Y. Wang, J. Liu, R. Wang, X. Li, M. Fang, G. Li, P. Rao and Y. Liu, *Ceram. Int.*, 2025, **51**, 60844–60854.
7 T. C. Dube and J. Zhang, *Ceram. Int.*, 2025, **51**, 47506–47515.
8 D. Guo, R. Jin, B. Shi, X. Jia, S. Wang and B. Xu, *Surf. Coat. Technol.*, 2025, **502**, 131994.
9 J. Y. Lu, Z. Q. Bu, Y. Q. Lei, D. Wang, B. He, J. Wang and W. T. Huang, *J. Mol. Liq.*, 2024, **409**, 125503.
10 N. Al-Harbi, H. Mohammed, Y. Al-Hadeethi, A. S. Bakry, A. Umar, M. A. Hussein, M. A. Abbassy, K. G. Vaidya, G. Al Berakdar, E. M. Mkawi and M. Nune, *Pharmaceuticals*, 2021, **14**, 75.
11 W. Chen, Y. Wang, J. Xu, X. Chen, O. B. Jensen, Q. Zhang and Z. Xia, *Laser Photon. Rev.*, 2024, **18**, 2300963.
12 Y. Zhang, S. Vardhaman, C. S. Rodrigues and B. R. Lawn, *J. Dent. Res.*, 2023, **102**, 245–253.
13 J. Kang, X. Yang, Q. Hu, Z. Cai, L. M. Liu and L. Guo, *Chem. Rev.*, 2023, **123**, 8859–8941.
14 P. S. Prakash, S. J. Pawar and R. P. Tewari, *Proc. Inst. Mech. Eng., Part L*, 2019, **233**, 1227–1240.
15 S. Ni, L. Chou and J. Chang, *Ceram. Int.*, 2007, **33**, 83–88.
16 K. O. Abdulwahab, M. M. Khan and J. R. Jennings, *ACS Omega*, 2023, **8**, 30802–30823.
17 Y. Zhuo, F. Wu, Y. Niu, Y. Wang, Q. zhang, Y. Teng, H. Dong and Z. Mu, *Laser Photon. Rev.*, 2024, **18**, 2400105.
18 N. T. Tasnim, N. Ferdous, M. M. H. Rumon and M. S. Shakil, *ACS Omega*, 2023, **9**, 16–32.
19 A. M. Mansour, B. A. Hemdan, A. Elzwawy, A. B. Abou Hammad and A. M. El Nahrawy, *Sci. Rep.*, 2022, **12**(1), 9855.
20 A. G. Boudjahem, S. Monteverdi, M. Mercy, D. Ghanbaja and M. M. Bettahar, *Catal. Letters*, 2002, **84**, 115–122.
21 A. M. EL Nahrawy, *Egypt. J. Chem.*, 2022, **65**, 115–139.
22 A. B. A. Hammad, A. M. Fathi, A. A. Azab, A. M. Mansour and A. M. El Nahrawy, *RSC Adv.*, 2025, **15**, 38969–38985.
23 A. M. Abouelnaga and A. B. Abou Hammad, *J. Solgel Sci. Technol.*, 2024, 1–10.
24 H. S. Magar, A. M. Mansour and A. B. A. Hammad, *Sci. Rep.*, 2024, **14**, 1849.
25 L. Yang and B. Kruse, *J. Opt. Soc. Am. A*, 2004, **21**, 1933.
26 R. Alcaraz de la Osa, I. Iparragirre, D. Ortiz and J. M. Saiz, *ChemTexts*, 2020, **6**, 2.
27 L. Jincheng, X. Bangyang, X. Lili, H. Yanying, L. Panpan, L. Tiesong, H. Peng and Y. Weiqi, *J. Eur. Ceram. Soc.*, 2022, **42**, 3708–3719.
28 J. Jeevanandam, M. Gonçalves, R. Castro, J. Gallo, M. Bañobre-López and J. Rodrigues, *Mater. Today Bio*, 2025, **31**, 101520.
29 A. Zandonà, V. Castaing, A. I. Shames, G. Helsch, J. Deubener, A. I. Becerro, M. Allix and A. Goldstein, *J. Non. Cryst. Solids*, 2023, **603**, 122094.
30 C. Büchner and M. Heyde, *Prog. Surf. Sci.*, 2017, **92**, 341–374.
31 G. Petcu, E. M. Anghel, I. Atkinson, D. C. Culita, N. G. Apostol, A. Kuncser, F. Papa, A. Baran, J. L. Blin and V. Parvulescu, *Gels*, 2024, **10**, 129.
32 R. J. Longbottom, Z. Wang, K. Hockings and B. J. Monaghan, *ISIJ Int.*, 2021, **61**, 2745–2753.
33 S. Khonthon, S. Morimoto and Y. Ohishi, *J. Optoelectron. Adv. Mater.*, 2007, **1**, 439–446.
34 J. Wang, X. Wang, C. Zhang, S. Lin, M. Dai, H. Wang, S. Xie and Q. Shi, *Sol. Energy Mater. Sol. Cells*, 2023, **257**, 112352.
35 M. R. B. Pirshahid, S. M. Alavi, M. Rezaei, E. Akbari, M. Varbar and K. Khosravi, *J. Energy Inst.*, 2023, **110**, 101361.
36 B. Vos, E. Poels and A. Bliek, *J. Catal.*, 2001, **198**, 77–88.
37 L. Liu, T. Liu, P. Liu, Q. Huang, H. Gui and A. Lu, *Ceram. Int.*, 2021, **47**, 32666–32674.
38 Z. Yin, L. Yi, F. Kong, Z. Chen, X. Fang, R. Zhang, Y. Chen, H. Jiang and C. Li, *J. Non. Cryst. Solids*, 2021, **568**, 120960.
39 J. N. Nouping Fekoua, P. Venyite, S. Bila, E. Kamseu, G. Bebga, M. Hanuskova, G. D. Poggetto, S. Rossignol and C. Leonelli, *Heliyon*, 2023, **9**, e17750.
40 R. Patidar, H. Gupta, A. Rahangdale and V. Jain, *Comput. Mater. Today*, 2025, **7**, 100034.
41 W. Thongthapthai, V. Harnchana, J. Sintusiri, P. Payakaniti, P. Thongbai and V. Amornkitbamrung, *Ceram. Int.*, 2024, **50**, 43098–43107.
42 C. Tianchi, C. Meili, X. Hao, Z. Longpeng, Z. Jialu and H. Ningning, *Colloids Surf., A*, 2021, **627**, 127002.
43 B. Li, S. Wang and Y. Fang, *J. Alloys Compd.*, 2017, **693**, 9–15.
44 W. Tang, Q. Zhang, Z. Luo, L. Han and A. Lu, *Silicon*, 2018, **10**(5), 2123–2128.
45 A. Dugué, L. Cormier, O. Dargaud, L. Galoisy and G. Calas, *J. Am. Ceram. Soc.*, 2012, **95**, 3483–3489.
46 M. A. Tena, R. Mendoza, J. R. García and S. García-Granda, *Results Phys.*, 2017, **7**, 1095–1105.
47 B. Wu, J. Qiu, M. Peng, J. Ren, X. Jiang and C. Zhu, *Mater. Res. Bull.*, 2007, **42**, 762–768.
48 Y. Wang, S. Bruyère, Y. Kumagai, N. Tsunoda, F. Oba, J. Ghanbaja, H. Sun, B. Dai and J. F. Pierson, *RSC Adv.*, 2022, **12**, 21940.

49 A. Dugué, O. Dymshits, L. Cormier, B. Cochain, G. Lelong, S. Belin and A. Zhilin, *J. Non. Cryst. Solids*, 2015, **413**, 24–33.
50 B. Wu, J. Qiu, M. Peng, J. Ren, X. Jiang and C. Zhu, *Mater. Res. Bull.*, 2007, **42**, 762–768.
51 M. G. Brik, N. M. Avram and C. N. Avram, *J. Optoelectron. Adv. Mater.*, 2006, **8**, 731–736.
52 F. Goga, R. Dudric, L. Bizo, A. Avram, A. Horatiu Marincas, C. J. Varhely and T. Dippong, *Stud. Univ. Babes-Bolyai, Chem.*, 2017, **1**, 261–270.
53 S. Zhou, H. Dong, H. Zeng, B. Wu, B. Zhu, H. Yang, S. Xu, Z. Wan and J. Qiu, *J. Appl. Phys.*, 2007, **102**, 063106.
54 K. Adaika, M. Diaifi and C. Liaidi, *Dig. J. Nanomater. Biostruct.*, 2021, **16**, 669–676.
55 S. Oudjertli, A. Mohammedi and M. Ibrir, *Solid State Phenom.*, 2022, **336**, 103–107.
56 A. C. Mohan, A. Athira, B. P. Nair, G. Sivasubramanian, K. M. Sreekanth, G. Anoop, S. P. Sree and K. M. Sreedhar, *Sci. Rep.*, 2024, **14**, 32067.
57 A. Mhamdi, B. Ouni, A. Amlouk, K. Boubaker and M. Amlouk, *J. Alloys Compd.*, 2014, **582**, 810–822.
58 M. Dehbashi and M. Aliahmad, *Int. J. Phys. Sci.*, 2012, **7**, 5415–5420.
59 P. Kaur, S. Rahul, K. Kaur, D. Arora, K. Asokan and D. Paul Singh, *Mater. Today Proc.*, 2020, **26**, 3436–3441.
60 V. Ivchenko, *Phys. Scr.*, 2024, **99**, 035952.
61 Z. M. Gibbs, A. Lalonde and G. J. Snyder, *New J. Phys.*, 2013, **15**, 075020.
62 C. S. Granerød, S. R. Bilden, T. Aarholt, Y. F. Yao, C. C. Yang, D. C. Look, L. Vines, K. M. Johansen and Ø. Prytz, *Phys. Rev. B*, 2018, **98**, 115301.
63 A. M. El Nahrawy, A. M. Mansour, A. B. Abou Hammad, R. S. Ibrahim, A. M. Abouelnaga and M. S. Abdel-Aziz, *J. Inorg. Organomet. Polym. Mater.*, 2020, **30**, 3084–3094.
64 A. M. El Nahrawy, A. Elzwawy, A. B. Abou Hammad and A. M. Mansour, *Solid State Sci.*, 2020, **108**, 106454.
65 A. M. El Nahrawy, A. B. Abou Hammad and A. M. Mansour, *ECS J. Solid State Sci. Technol.*, 2024, **13**, 104002.
66 A. Darwish, M. I. Farouk, M. Morsy and A. Elzwawy, *Nanoscale Adv.*, 2025, **7**, 5166–5183.
67 A. G. Darwish, M. I. Farouk, M. I. Abdelglil and H. A. Abo-Mosallam, *RSC Adv.*, 2025, **15**, 49699–49713.
68 S. Kumar, S. Kumari, V. Kumar, J. Dalal, A. Kumar and A. Ohlan, *J. Phys. Chem. Solids*, 2022, **170**, 110911.
69 A. A. Ali, A. G. Darwish and S. Ibrahim, *Ceram. Int.*, 2026, DOI: 10.1016/j.ceramint.2026.02.064.
70 M. Tijaria, Y. Sharma, V. Kumar, S. Dahiya and J. Dalal, *Mater. Today Proc.*, 2021, **45**, 3722–3725.
71 A. K. Jonscher, *Nature*, 1977, **267**, 673–679.
72 V. Koval, G. Viola, M. Zhang, M. Faberova, R. Bures and H. Yan, *J. Eur. Ceram. Soc.*, 2024, **44**, 2886–2902.
73 A. B. Abou Hammad, A. G. Darwish and A. M. El Nahrawy, *Appl. Phys.*, 2020, **126**, 504.
74 K. R. Ketab and H. H. Mihsen, *Chem. Afr.*, 2024, **8**(1), 325–336.
75 M. M. Naik, H. S. B. Naik, G. Nagaraju, M. Vinuth, K. Vinu and S. K. Rashmi, *J. Mater. Sci.: Mater. Electron.*, 2018, **29**, 20395–20414.
76 O. Choi and Z. Hu, *Environ. Sci. Technol.*, 2008, **42**, 4583–4588.
77 G. Wang, W. Jin, A. M. Qasim, A. Gao, X. Peng, W. Li, H. Feng and P. K. Chu, *Biomaterials*, 2017, **124**, 25–34.
78 O. Chikelu, M. Ezeibe, G. Anosa, O. Okorie, N. Elendu-Eleke, O. Okoroafor and A. Ngene, *Nature Precedings*, 2012, DOI: 10.1038/npre.2012.6814.1.
79 K. Karthik, S. Dhanuskodi, C. Gobinath, S. Prabukumar and S. Sivaramakrishnan, *J. Photochem. Photobiol. B*, 2019, **190**, 8–20.
80 J. Gajendiran, J. R. Ramya, R. Vijayalakshmi, P. Balraju, R. Suresh, G. Thennarasu and L. Gnanasekaran, *Inorg. Chem. Commun.*, 2025, **181**, 115163.
81 A. Yusuf, S. Al Jitan, C. Garlisi and G. Palmisano, *Chemosphere*, 2021, **278**, 130440.
82 E. Absi, N. M. Al Hada, J. H. Ibbini, D. Alrousan, N. E. Ahmad, K. Jamaluddin, M. A. Saleh and K. Hamzah, *Ceram. Int.*, 2025, **51**, 5940–5954.
83 N. Verma, S. Vaidh, G. S. Vishwakarma and A. Pandya, *Nanotoxicity: Prevention and Antibacterial Applications of Nanomaterials*, 2020, pp. 365–383.
84 O.-M. Goudouri, E. Kontonasaki, U. Lohbauer and A. R. Boccaccini, *Acta Biomater.*, 2020, DOI: 10.1016/j.actbio.2014.03.028.
85 S. Ramanathan, S. C. B. Gopinath, M. K. M. Arshad and P. Poopalan, *J. Cleaner Prod.*, 2020, **253**, 119923.
86 R. Al-Gaashani, V. Kochkodan, M. Pasha, A. M. Al-Emadi, Y. Tong and Y. Manawi, *Results Eng.*, 2026, **29**, 109103.
87 J. S. Santos, V. Márquez, J. G. Buijnsters, S. Praserthdam and P. Praserthdam, *Appl. Surf. Sci.*, 2023, **607**, 155072.